TXN, a Xanthohumol Derivative, Attenuates High-Fat Diet Induced Hepatic Steatosis by Antagonizing PPARγ

Yang Zhang[1*], Gerd Bobe[2], Cristobal L. Miranda[3], Malcolm B. Lowry[4], Victor L. Hsu[5], Christiane V. Löhr[6], Carmen P. Wong[1], Donald B. Jump[1], Matthew M. Robinson[7], Thomas J. Sharpton[8], Claudia S. Maier[9], Jan F. Stevens[3], Adrian F. Gombart[10*]

[1]School of Biological and Population Health Sciences, Nutrition Program, Linus Pauling Institute, Oregon State University, Corvallis, OR 97331, USA

[2]Department of Animal Sciences, Linus Pauling Institute, Oregon State University, Corvallis, OR 97331, USA

[3]Department of Pharmaceutical Sciences, Linus Pauling Institute, Oregon State University, Corvallis, OR 97331, USA

[4]Department of Microbiology, Oregon State University, Corvallis, OR 97331, USA

[5]Department of Biochemistry and Biophysics, Oregon State University, Corvallis, OR 97331, USA

[6]Department of Biomedical Science, Carlson College of Veterinary Medicine, Corvallis, OR 97331, USA

[7]School of Biological and Population Health Sciences, Kinesiology Program, Oregon State University, Corvallis, OR 97331, USA

[8]Department of Microbiology, Department of Statistics, Oregon State University, Corvallis, OR 97331, USA

[9]Department of Chemistry, Linus Pauling Institute, Oregon State University, Corvallis, OR 97331, USA

[10]Linus Pauling Institute, Department of Biochemistry and Biophysics, Oregon State University, Corvallis, OR 97331, USA

[*]Authors to whom correspondence should be addressed.

Abstract

We previously reported xanthohumol (XN), and its synthetic derivative tetrahydro-XN (TXN) attenuates high-fat diet (HFD) induced obesity and metabolic syndrome in C57BL/6J mice. The objective of the current study was to determine the effect of XN and TXN on lipid accumulation in the liver. Non-supplemented mice were unable to adapt their caloric intake to 60% HFD, resulting in obesity and hepatic steatosis; however, TXN reduced weight gain and decreased hepatic steatosis. Liver transcriptomics indicated TXN might antagonize lipogenic PPARγ actions *in vivo*. XN and TXN inhibited rosiglitazone-induced 3T3-L1 cell differentiation concomitant with decreased expression of lipogenesis-related genes. A PPARγ competitive binding assay showed XN and TXN bind to PPARγ with an IC_{50} similar to pioglitazone and 8-10 times stronger than oleate. Molecular docking simulations demonstrated XN and TXN bind in the PPARγ ligand-binding domain pocket. Our findings are consistent with XN and TXN acting as antagonists of PPARγ.

Introduction

Non-alcoholic fatty liver disease (NAFLD) is a major global health threat characterized by excessive hepatic lipid droplet accumulation with a history of little or no alcohol consumption (Hashimoto, Taniai and Tokushige, 2013). About one-quarter of the US population suffers from NAFLD (Estes *et al.*, 2018) with rates in the rest of the world ranging from 14% in Africa to 32% in the Middle East (Younossi *et al.*, 2016). The continuing obesity and diabetes epidemic drives increasing rates of NAFLD (Estes *et al.*, 2018). Unfortunately, no FDA-approved drugs exist for its treatment. Sustained healthy life style changes and weight loss are the only interventions proven effective in preventing the onset and progression of NAFLD (Stefan, Häring and Cusi, 2019). Thus, there is a critical need for novel and effective interventions.

As a central hub for lipid metabolism, a healthy liver maintains homeostasis among uptake, esterification, oxidation and secretion of fatty acids (FAs) (Goldberg and Ginsberg, 2006). Overconsumption of saturated FAs or sugars can overload the liver, disrupt lipid homeostasis, resulting in excess storage of triacylglycerols (TAG) in hepatocytes and the onset and progression of hepatic steatosis (Ipsen, Lykkesfeldt and Tveden-Nyborg, 2018). Given that PPARγ is important in hepatic lipogenesis (Sharma and Staels, 2007), it has attracted

55 considerable attention as a therapeutic target for NAFLD (Almeda-Valdés, Cuevas-Ramos and
56 Aguilar-Salinas, 2009).

57 Attenuated PPARγ activity in heterozygous PPARγ-deficient (*PPARγ*$^{+/-}$) C57BL/6J mice
58 protects against HFD-induced obesity, liver steatosis and adipocyte hypertrophy; however,
59 treatment with the PPARγ agonist pioglitazone (PGZ) abrogates the protection against
60 hypertrophy and decreases insulin sensitivity (Kubota *et al.*, 1999) suggesting a potential
61 beneficial use for PPARγ antagonists to treat hepatic steatosis. PPARγ antagonists tanshinone
62 IIA (Gong *et al.*, 2009), β-cryptoxanthine (Goto *et al.*, 2013), protopanaxatriol (Zhang *et al.*,
63 2014), isorhamnetin (Zhang *et al.*, 2016), and Gleevec (Choi *et al.*, 2016) improved multiple
64 metabolic parameters in diet-induced obese (DIO) mice. These observations strongly suggest that
65 moderate inhibition of PPARγ activity may reduce the risk for developing hepatic steatosis
66 induced by diet, and PPARγ antagonists may be useful for the treatment and prevention of
67 NAFLD.

68 Xanthohumol (XN), a prenylated flavonoid found in hops (*Humulus lupulus* L.),
69 improves multiple parameters of MetS in rat and mouse models (Legette *et al.*, 2014; Miranda *et*
70 *al.*, 2016, 2018). Tetrahydroxanthohumol (TXN), a non-estrogenic synthetic XN derivative (**Fig.**
71 **1**), appears more effective in ameliorating MetS in DIO mice than XN possibly due to its 5-, 10-,
72 and 12-fold higher levels in the muscle, plasma and liver, respectively, as compared with XN
73 (Miranda *et al.*, 2018). Both compounds likely mediate their benefits via multiple mechanisms.
74 XN inhibits differentiation of preadipocytes and induces apoptosis in mature adipocytes (Yang *et*
75 *al.*, 2007; Rayalam *et al.*, 2009), attenuates the function of SREBP-1 by repressing its maturation
76 (Miyata *et al.*, 2015) and induces beiging of white adipose tissue, decreases adipogenesis, and
77 induces lipolysis (Samuels, Shashidharamurthy and Rayalam, 2018). We recently showed that
78 XN and TXN significantly change gut microbiota diversity and abundance, alter bile acid
79 metabolism and reduce inflammation in mice fed a HFD (Zhang *et al.*, 2020). Collectively, these
80 data suggest both XN and TXN are effective for treatment of metabolic disorders and are
81 promising candidates for NAFLD prevention and treatment.

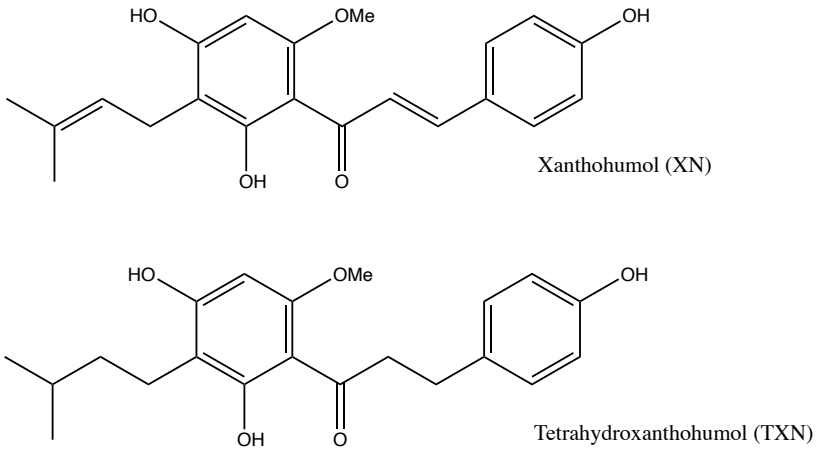

Figure 1. Structures of XN and its synthetic derivative TXN.

In the present study, we show a daily oral intake of TXN at 30 mg/kg body weight (BW) or XN at a daily dose of 60 mg/kg BW strongly suppresses diet-induced liver steatosis in C57BL/6J male mice. Supervised machine learning of liver RNA-seq data identified perturbations in PPARγ signaling. Based on cell culture experiments, a PPARγ competitive binding assay and molecular docking studies, we provide evidence that XN and TXN act as novel PPARγ antagonists with moderate binding activity. Collectively, our findings suggest appropriate functional antagonism of PPARγ is a logical approach to prevent and treat diet-induced liver steatosis and other related metabolic disorders. The structures of XN and TXN could serve as scaffolds for synthesis of more effective compounds to treat NAFLD.

Results

1. TXN attenuates HFD-induced weight gain independent of caloric intake

As expected, C57BL/6J mice on a 60% HFD (**Fig. 2A**, solid blue line) gained more BW than mice on the LFD (**Fig. 2A**, dotted black line) throughout the experimental period (week 1: $p < 0.05$; week 2-16: $p < 0.001$; repeated measures). TXN-supplementation (**Fig. 2A**, solid dark green line) attenuated HFD-induced BW gain throughout the experimental period (week 1: $p < 0.05$; week 2-16: $p < 0.001$; repeated measures). XN supplementation showed a dose response effect: the higher dosage (HXN; **Fig. 2A**, solid red line), but not the lower dosage (LXN; **Fig. 2A**, solid yellow line), attenuated HFD-induced BW gain between week 8 and 16. When BW gain was expressed as % of initial BW, HFD-fed mice almost doubled their initial BW (+98.3 ±

103 2.7%), whereas TXN-treated mice gained 33% less (+66.2 ± 5.8%, $p < 0.0001$), and LFD-fed
104 mice gained 53% less (+45.8 ± 4.3%, $p < 0.0001$) than HFD-fed mice (**Fig. 2B**). Although not
105 statistically significant, both LXN- and HXN-treated mice gained 7.5% and 11% less,
106 respectively (90.0 ± 3.3%, $p = 0.20$; 87.6 ± 3.9%, $p = 0.07$; **Fig. 2B**). In male C57BL/6J mice, a
107 BW of approximately 40 g is a critical tipping point from which metabolic dysfunction occurs
108 (van Beek *et al.*, 2015). After 16 weeks, mean BW for these mice was LFD (37.5 ± 1.1g), HFD
109 (50.3 ± 0.6g), LXN (49.9 ± 1.1g), HXN (47.4 ± 1.1g) and TXN (42.2 ± 1.6g).

110 Overtime, mice adapted to the HFD by consuming less food than LFD-fed mice (**Fig.**
111 **2C**). However, the discrepancy in food consumption was insufficient to counteract the elevated
112 caloric intake (**Fig. 2D**). HXN-treated mice adapted better to the HFD, indicated by decreased
113 food intake at week 1, 6-10, 13, and 16 ($p < 0.05$), and caloric intake ($p = 0.01$) (**Fig. 2C-D**),
114 resulting in less BW gain. In contrast, the attenuated BW gain in TXN-treated mice was not
115 accompanied by a significant reduction in food or caloric intake (**Fig. 2C-D**).

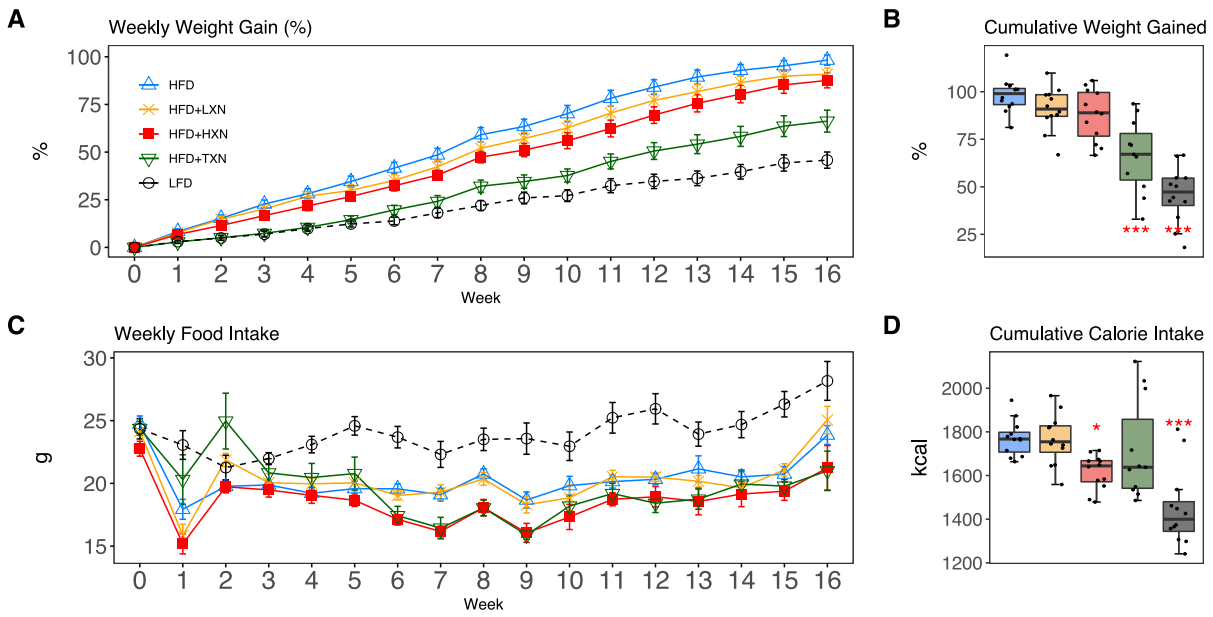

Figure 2. TXN and HXN suppress HFD-induced BW gain independent of caloric intake. Mice were fed either a LFD (black dashed line with empty circles, n = 12), a HFD (blue solid line with empty triangles, n = 12), HFD+LXN (yellow solid line with crosses, n = 12), HFD+HXN (red solid line with squares, n = 12), or HFD+TXN (green solid line with empty triangles, n = 11) for 16 weeks. (A) BW gain was assessed once per week. Data is expressed as means ± SEM. Repeated measurement of ANOVA was used to calculate *p*-values for the percentage of weight gained weekly. (B) Total percent BW gained at the end of the16-week feeding period. Data is expressed as quartiles. (C) Food intake was assessed once per week during the 16-week feeding period. Data is expressed as means ± SEM. Repeated measurement of ANOVA was used to calculate *p*-values for weekly food intake. (D) Total calories consumed at the end of 16-week feeding period. Data are expressed as quartiles. Source files of data used for the analysis and visualization are available in the Figure 2—source data 1.

Figure 2—source data 1

Source files.

This zip archive contains the following:

1) One Comma Separated Values file named “phenome_feeding.csv” contains food intake and weight entries.

2) One Excel workbook named “2019TXN_repeated_measures_YZGB.xlsx” contains repeated measures analyses.

3) The Jupyter Notebook contains scripts used for statistical analysis and generation of Fig. 2.

136 **2. TXN attenuates hepatic steatosis and HFD-induced obesity**

137 HFD-induced BW gain was primarily body fat accumulation, as indicated by measurements
138 obtained from DEXA scans. HFD mice had greater fat mass than LFD mice ($p < 0.0001$; **Fig.**
139 **3A**). Linear regression of total fat mass to total caloric intake revealed a strong relationship
140 between caloric intake and fat mass among groups (r = +0.52; $p < 0.0001$) and within LFD-fed
141 mice (r = +0.79; $p = 0.002$; **Fig. 3A1**). In contrast, caloric intake was not correlated to fat mass in
142 any HFD group (**Fig. 3A2-5**), indicating a disconnection between caloric intake and fat mass
143 after prolonged HFD consumption. Supplementation with HXN (-9.93%; $p < 0.05$) and even
144 more so with TXN (-27.7%; $p < 0.001$) decreased body fat mass on HFD (**Fig. 3A**), indicating
145 that HXN and TXN attenuated the HFD-induced body fat accumulation and that this effect was
146 not explained by changes to caloric intake (**Fig. 3A4-5**).

147 Hepatic steatosis was measured by percent surface area occupied by lipid vacuoles in
148 formalin-fixed, paraffin-embedded liver by image analysis of photomicrographs. In the absence
149 of supplementation, HFD- and LFD-fed mice shared similar hepatic lipid areas (**Fig. 3B**). Caloric
150 intake was positively correlated with hepatic lipid area on both LFD-fed mice (r = +0.61, $p =$
151 0.03; **Fig. 3B1**) and a HFD (r = +0.57, $p = 0.05$; **Fig. 3B2**). Supplementation with HXN ($p <$
152 0.05) and TXN ($p < 0.01$) mitigated hepatic steatosis, independent of caloric intake (**Fig. 3B4-5**).

153 Changes in energy balance may drive changes in obesity-related steatosis. We
154 investigated TXN on whole-body energy metabolism to determine mechanisms of TXN
155 protection from weight gain, which can influence steatosis. Towards the end of the study, we
156 measured whole-body expenditure for all 59 mice using a computer-controlled indirect
157 calorimetry system (metabolic cages). Energy expenditure was calculated from the oxygen and
158 carbon dioxide exchange ratio using the Weir equation (Weir, 1949). Total energy expenditure
159 contains energy expenditure for basal metabolism, body tissue synthesis, digestion, and physical
160 activity (Speakman, 2013). Mice consuming HFD and mice supplemented with LXN had higher
161 ($p < 0.05$) energy expenditure than mice on LFD, HXN and TXN (**Fig. 3C**). Caloric intake was
162 positively correlated with energy expenditure in LFD- (**Fig. 3C1**), LXN- (**Fig. 3C3**), HXN- (**Fig.**
163 **3C4**) and TXN-fed mice (**Fig. 3C5**) but was not correlated with energy expenditure in HFD mice
164 (**Fig. 2C2**). We investigated the influence of body mass on energy expenditure using analysis of
165 covariance (ANCOVA) of body mass upon entry into the cages between diets (Tschöp *et al.*,

2011). ANCOVA revealed that LXN, HXN, or TXN supplementation did not change the positive relationship between energy expenditure and body mass (**Figure 3—figure supplement 1**).

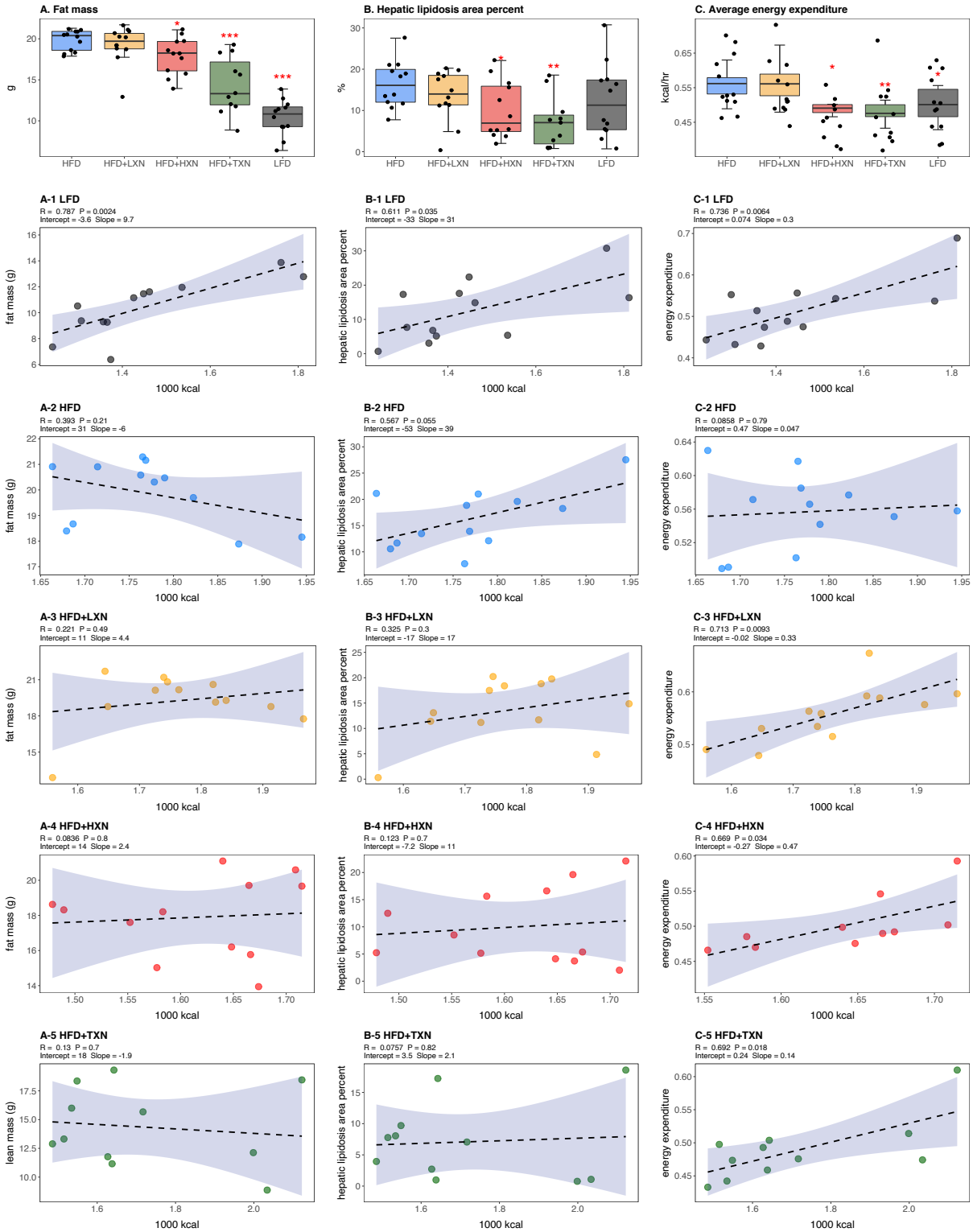

Figure 3. Energy homeostasis imbalance induced by HFD is prevented by XN and TXN supplementation. Mice were fed either a LFD (black, n = 12), a HFD (blue, n = 12), HFD+LXN (yellow, n = 12), HFD+HXN (red, n = 12), or HFD+TXN (green, n = 11) for 16 weeks. (A) Total fat mass measured by DXA scan two days prior to necropsy is expressed as quartiles. (A-1) Relationship between total fat mass and total caloric intake over 16 weeks of feeding for LFD; (A-2) HFD; (A-3) HFD+LXN; (A-4) HFD+HXN; and (A-5) HFD+TXN groups. (B) Hepatic lipidosis area percent expressed as quartiles. (B-1) Relationship between hepatic lipidosis area percent and total caloric intake over 16 weeks of feeding for LFD; (B-2) HFD; (B-3) HFD+LXN; (B-4) HFD+HXN; and (B-5) HFD+TXN groups. (C) Average energy expenditure over two light-dark cycles (48 hours) obtained using metabolic cages and expressed as quartiles. (C-1) Relationship between energy expenditure and total caloric intake over 16 weeks of feeding for LFD; (C-2) HFD; (C-3) HFD+LXN; (C-4) HFD+HXN (with removal of two outliers); (C-5) for HFD+TXN groups. Pre-planned general linear model with contrasts were used to calculate *p*-values in A, B and C. $*p < 0.05$, $**p < 0.01$, $***p < 0.001$. Linear regression analyses of total calories versus total fat mass (A1-5), hepatic lipidosis area percent (B1-5), and average energy expenditure (C1-5) in mice were done using stats package version 3.6.2 in R. Blue shading represents 95% CI of the regression line. Absolute value of R, p-value, intercept, and slope for the regression are reported above each corresponding panel. Source files of data used for the analysis are available in the Figure 3—source data 1.

Figure 3—source data 1

Source files.

This zip archive contains the following:

1) One Comma Separated Values file named “metabolicGasExchange.csv” contains metabolic cage gas exchange data.

2) One Comma Separated Values file named “fig3_table.csv” contains phenotypic data directly pertaining to Fig. 3.

3) A Jupyter Notebook file contains scripts used for statistical analysis and generation of Fig. 3.

4) An R script file “ggplotRegression.R”

5) A folder named “Fig3Sup1” containing Figure 3—figure supplement 1.

    a. One Comma Separated Values file named “metabolicGasExchange.csv” contains metabolic cage gas exchange data.

    b. One Comma Separated Values file named “supplement1Table.csv” contains phenotypic data directly pertaining to Figure 3—figure supplement 1.

    c. An R script file “ggplotRegression.R.

    d. A Jupyter Notebook file contains scripts used for statistical analysis and generation of figure supplement 1.

    e. A pdf file named “fig3Sup1.pdf”.

f. A word document named “fig3Sup1.docx” containing the figure and figure legend.

6) A folder named “Fig3Sup2” containing Figure 3—figure supplement 2.

a. One Comma Separated Values file named “supplement2Table.csv” contains phenotypic data directly pertaining to Figure 3—figure supplement 2.

b. An R script file “ggplotRegression.R.

c. A Jupyter Notebook file contains scripts used for statistical analysis and generation of figure supplement 2.

d. A pdf file named “fig3Sup2.pdf”.

e. A word document named “fig3Sup2.docx” containing the figure and figure legend.

215 As a marker of hepatic lipid uptake and export, fasting plasma TAG level was measured
216 at the end of the study. Similar to hepatic lipid area, fasting plasma TAG did not reflect the
217 caloric density of the diet (**Fig. 3—figure supplement 2**); namely, there was an inverse
218 relationship between caloric intake and plasma TAG among LFD mice (Spearman, r = -0.60, p =
219 0.04; **Fig. 3—figure supplement 2 A1**), which was lost on the HFD (Spearman, r = 0.12, p =
220 0.70; **Fig. 3—figure supplement 2 A2**). TXN treatment restored the negative correlation
221 between caloric intake and plasma TAG (Spearman r = -0.65, p = 0.04; **Fig. 3—figure**
222 **supplement 2 A5**). One explanation for the higher plasma TAG ($p < 0.01$) observed could be
223 that TXN inhibited hepatic lipid uptake, and promoted hepatic lipid export, or both. TAG levels
224 remained in the normal physiological range (40 to 60 mg/dL) for all groups (Bogue *et al.*, 2020).
225 We collected fecal pellets over a 3-day period and measured fecal TAG at the end of the
226 study as an indicator of fecal energy excretion. Fecal TAG levels did not differ among all groups
227 (**Fig. 3—figure supplement 2 B**). No relationship was observed between caloric intake and fecal
228 TAG among or within groups (**Fig. 3—figure supplement 2 B1-5**), suggesting that the
229 attenuated BW gain and hepatic steatosis in TXN- and HXN-treated mice was not related to
230 increased fecal TAG excretion.

231 **3. Effects of XN and TXN on food intake frequency, physical activity and energy**
232 **expenditure**

233 We considered if physical activity level could explain attenuated weight gain of XN- and TXN-
234 treated groups. We differentiated activity measured in the metabolic cages into directed
235 ambulatory locomotion (sum of all locomotion of 1 cm/second or above within the x, y beam-
236 break system) (**Fig. 4A**) and fine movements (e.g., grooming, nesting and scratching) (**Fig. 4B**).
237 In addition, we approximated the ambulatory movement for food consumption by measuring
238 feeding frequency (**Fig. 4C**). In contrast to energy expenditure (**Fig. 4C**), directed ambulatory
239 locomotion was lower in HFD- than LFD-fed mice (**Fig. 4A**), while fine movement level (**Fig.**
240 **4B**) and feeding frequency (**Fig. 4C**) were not changed. TXN-treated mice exhibited higher
241 directed ambulatory locomotion and fine movement levels than HFD mice (**Fig. 4A, B**), whereas
242 feeding frequency was unchanged (**Fig. 4C**). XN-treated HFD mice showed higher directed
243 ambulatory locomotion activity and feeding frequency than HFD mice (**Fig. 4A, C**), whereas
244 fine movement activity levels were not affected (**Fig. 4B**).

245 In HFD-fed and LXN-treated mice, directed ambulatory locomotion levels were
246 positively correlated with food frequency (**Fig. 4C2-3**) but negatively correlated with energy
247 expenditure (**Fig. 4A2-3**), suggesting that food-driven activity may account for a major part of
248 total directed ambulatory motion and that these mice spent the majority of their time and energy
249 moving around for food consumption. In summary, HFD-fed mice used more energy for
250 maintaining basal metabolism, body tissue turnover, or digestion as indicated by a higher energy
251 expenditure and lower directed ambulatory locomotion activity than LFD mice. Compared to
252 HFD only mice, XN- and TXN-treated mice had lower energy expenditure and higher directed
253 ambulatory locomotion and fine movement activities, indicating lower energy for maintaining
254 basal metabolism, body tissue turnover, or digestion and remained more physically active than
255 untreated HFD-fed mice.

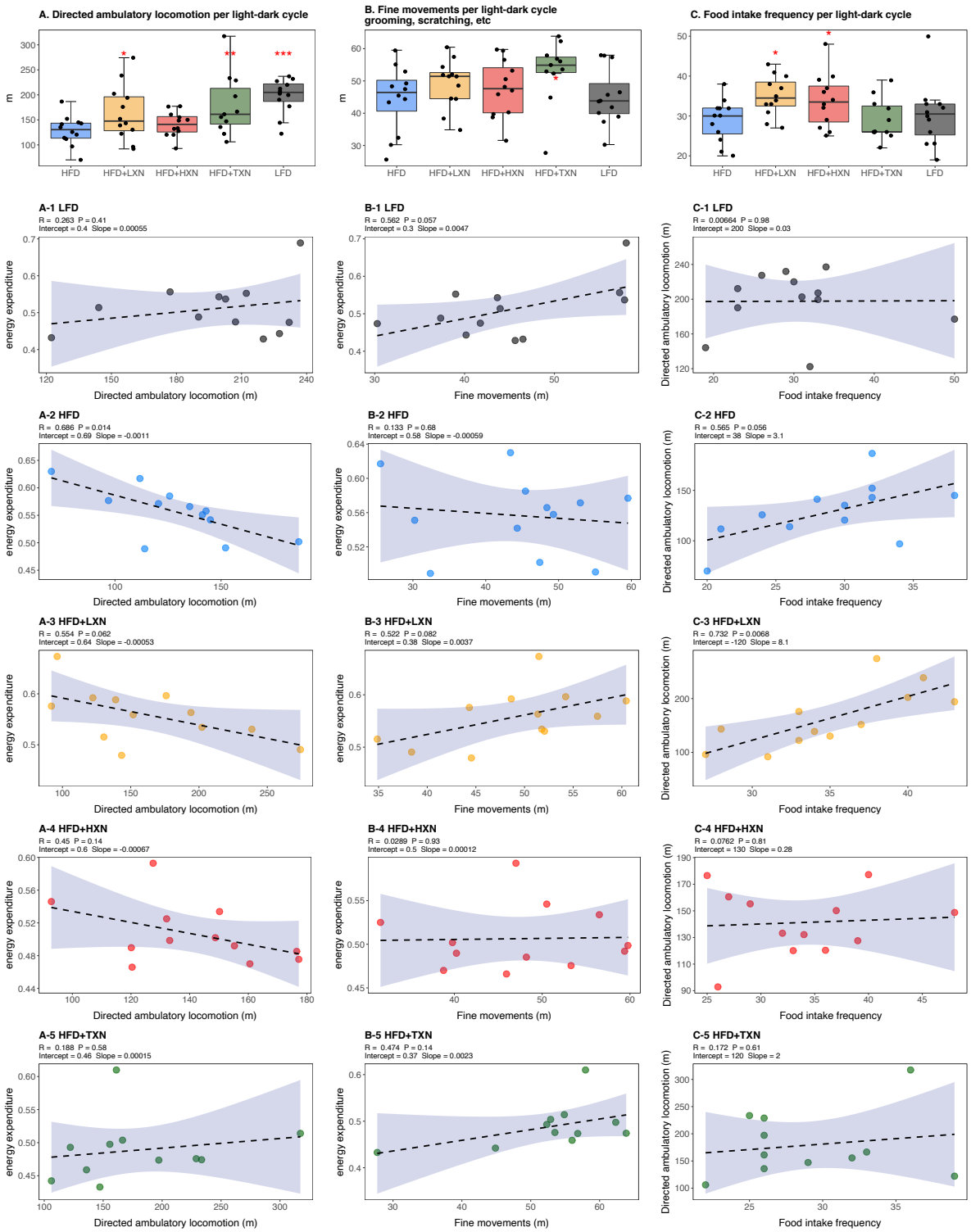
A. Directed ambulatory locomotion per light-dark cycle
B. Fine movements per light-dark cycle grooming, scratching, etc
C. Food intake frequency per light-dark cycle
m
HFD
HFD+LXN
HFD+HXN
HFD+TXN
LFD
A-1 LFD
R = 0.263 P = 0.41
Intercept = 0.4 Slope = 0.00055
B-1 LFD
R = 0.562 P = 0.057
Intercept = 0.3 Slope = 0.0047
C-1 LFD
R = 0.00664 P = 0.98
Intercept = 200 Slope = 0.03
A-2 HFD
R = 0.686 P = 0.014
Intercept = 0.69 Slope = -0.0011
B-2 HFD
R = 0.133 P = 0.68
Intercept = 0.58 Slope = -0.00059
C-2 HFD
R = 0.565 P = 0.056
Intercept = 38 Slope = 3.1
A-3 HFD+LXN
R = 0.554 P = 0.062
Intercept = 0.64 Slope = -0.00053
B-3 HFD+LXN
R = 0.522 P = 0.082
Intercept = 0.38 Slope = 0.0037
C-3 HFD+LXN
R = 0.732 P = 0.0068
Intercept = -120 Slope = 8.1
A-4 HFD+HXN
R = 0.45 P = 0.14
Intercept = 0.6 Slope = -0.00067
B-4 HFD+HXN
R = 0.0289 P = 0.93
Intercept = 0.5 Slope = 0.00012
C-4 HFD+HXN
R = 0.0762 P = 0.81
Intercept = 130 Slope = 0.28
A-5 HFD+TXN
R = 0.188 P = 0.58
Intercept = 0.46 Slope = 0.00015
B-5 HFD+TXN
R = 0.474 P = 0.14
Intercept = 0.37 Slope = 0.0023
C-5 HFD+TXN
R = 0.172 P = 0.61
Intercept = 120 Slope = 2
energy expenditure
Directed ambulatory locomotion (m)
Fine movements (m)
Food intake frequency

256

Figure 4. Effects of XN and TXN on food intake frequency, physical activity and energy expenditure. Mice were fed either a LFD (black, n = 12), a HFD (blue, n = 12), HFD+LXN (yellow, n = 12), HFD+HXN (red, n = 12), or HFD+TXN (green, n = 11) for 16 weeks. (A) Directed ambulatory locomotion per 24-hour cycle obtained using a computer controlled indirect calorimetry system. Data expressed as quartiles. (A-1) Relationship between directed ambulatory locomotion and energy expenditure for LFD; (A-2) HFD; (A-3) HFD+LXN; (A-4) HFD+HXN and (A-5) HFD+TXN groups. (B) Fine movements per 24-hour cycle calculated by subtracting directed ambulatory locomotion from sum of all distances traveled within the beam-break system. Data is expressed as quartiles. (B-1) Relationship between fine movements and energy expenditure for LFD; (B-2) HFD; (B-3) HFD+LXN; (B-4) HFD+HXN; and (B-5) HFD+TXN groups. (C) Number of food intake events recorded in metabolic cages. Data expressed as quartiles. (C-1) Relationship between number of food intake events and directed ambulatory locomotion for LFD; (C-2) HFD; (C-3) HFD+LXN; (C-4) HFD+HXN; (C-5) for HFD+TXN groups. Pre-planned general linear model with contrasts were used to calculate *p*-values in A, B and C. $*p < 0.05$, $**p < 0.01$, $***p < 0.001$. Linear regression analyses of energy expenditure versus directed ambulatory locomotion (A1-5), fine movements (B1-5), and directed ambulatory locomotion and number of food intake events (C1-5) in mice were done using stats package version 3.6.2 in R. Blue shading represents 95% CI of the regression line. Absolute value of R, p-value, intercept, and slope for the regression are reported above each corresponding panel. Source files of data used for the analysis are available in the Figure 4—source data 1.

Figure 4—source data 1

Source files.

This zip archive contains the following:

1) One Comma Separated Values file named “fig4_table.csv” phenotypic data directly pertaining to Fig. 4.
2) An R script file “ggplotRegression.R”.
3) A Jupyter Notebook file contains scripts used for statistical analysis and generation of Fig. 4.

286 **4. TXN attenuates HFD-induced lipid accumulation in white adipose tissue (WAT)**
287 To assess the effect of XN and TXN on lipid accumulation, fat pads from three distinct sites:
288 subcutaneous (sWAT), epididymal (eWAT), and mesenteric (mWAT) adipose tissue were
289 carefully removed and weighed during necropsy. Diet-induced lipid accumulation differed by
290 adipose site. Compared to the LFD, the HFD-induced increase in mWAT fat mass was much
291 greater than the increase in sWAT fat mass (three-fold vs. 2.5-fold increase, respectively), with
292 the smallest increase (15%) observed in eWAT fat mass (**Fig. 5A, C**). Supplementation with
293 HXN ($p < 0.05$), and even more so TXN ($p < 0.0001$), decreased sWAT and mWAT fat mass. A
294 smaller but significant increase in eWAT adipose tissue weight was observed in HXN- and
295 TXN-treated mice (**Fig. 5B**).
296 Caloric intake across diets was positively correlated with sWAT (r = +0.47; $p = 0.0002$;
297 **Fig. 5A**) and mWAT fat mass (r = +0.39; $p = 0.002$; **Fig. 5C**), but no relationship was observed
298 within XN- or TXN-treated groups (**Fig. 5A3-5, C3-5**), indicating lipid accumulation in sWAT
299 and mWAT fat depots was primarily linked to diet rather than the amount of food consumed. In
300 eWAT adipose depot, we observed the opposite. Unlike sWAT and mWAT fat depots, caloric
301 intake across diets was not correlated with eWAT fat mass (r = +0.03; $p = 0.82$; **Fig. 5B**).
302 Instead, a positive correlation between caloric intake and eWAT fat mass was found within LFD-
303 fed mice (**Fig. 5B1**), and a negative correlation between caloric intake and eWAT fat mass was
304 observed in both XN- and TXN-treated mice (**Fig. 5B3-5**). No correlation was found in HFD-fed
305 control mice (**Fig. 5B2**). These observations are consistent with distinct WAT depots in mice
306 differing in expandability (van Beek *et al.*, 2015).

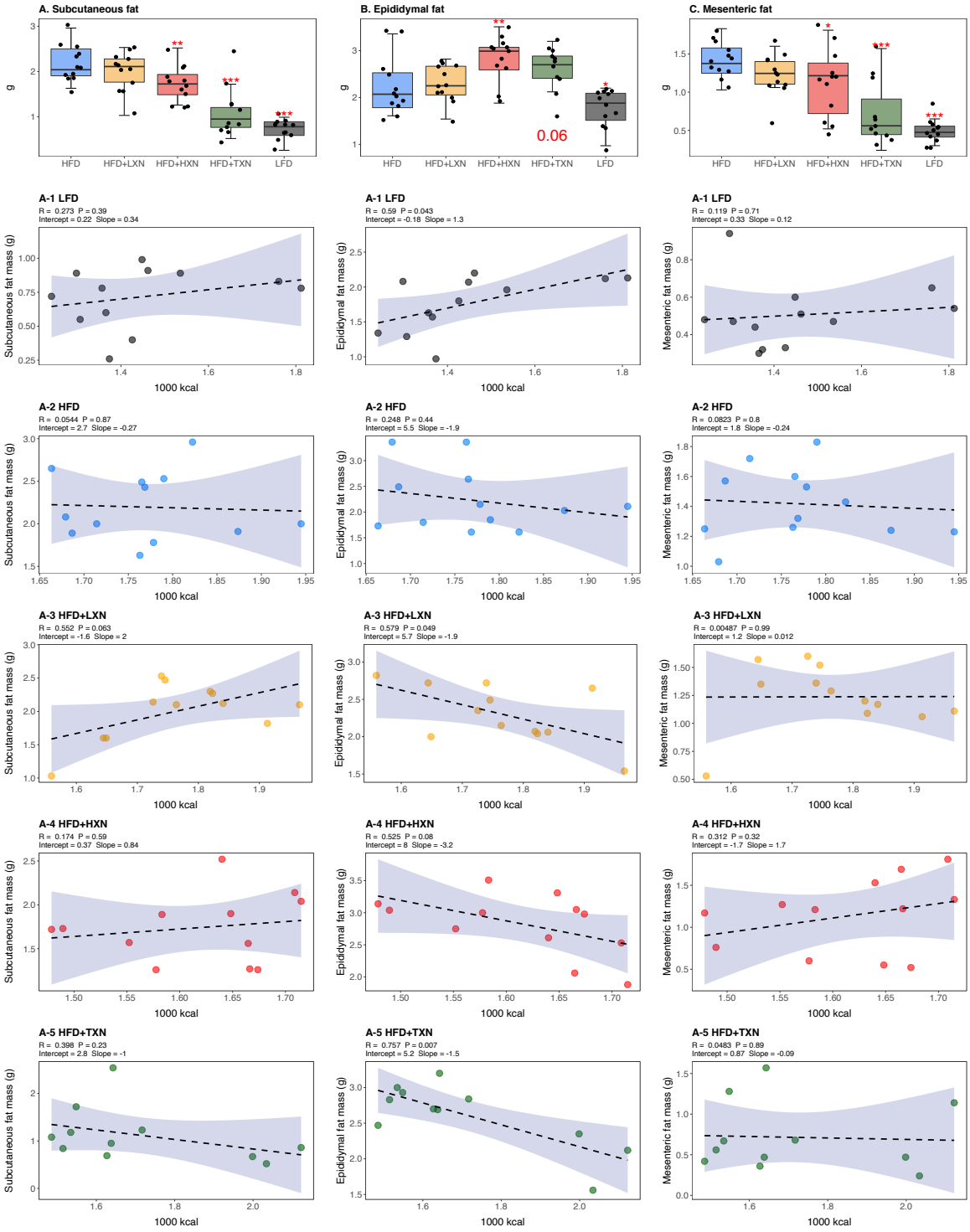
A. Subcutaneous fat
B. Epididymal fat
C. Mesenteric fat
g
HFD
HFD+LXN
HFD+HXN
HFD+TXN
LFD
0.06
A-1 LFD
R = 0.273 P = 0.39
Intercept = 0.22 Slope = 0.34
R = 0.59 P = 0.043
Intercept = -0.18 Slope = 1.3
R = 0.119 P = 0.71
Intercept = 0.33 Slope = 0.12
A-2 HFD
R = 0.0544 P = 0.87
Intercept = 2.7 Slope = -0.27
R = 0.248 P = 0.44
Intercept = 5.5 Slope = -1.9
R = 0.0823 P = 0.8
Intercept = 1.8 Slope = -0.24
A-3 HFD+LXN
R = 0.552 P = 0.063
Intercept = -1.6 Slope = 2
R = 0.579 P = 0.049
Intercept = 5.7 Slope = -1.9
R = 0.00487 P = 0.99
Intercept = 1.2 Slope = 0.012
A-4 HFD+HXN
R = 0.174 P = 0.59
Intercept = 0.37 Slope = 0.84
R = 0.525 P = 0.08
Intercept = 8 Slope = -3.2
R = 0.312 P = 0.32
Intercept = -1.7 Slope = 1.7
A-5 HFD+TXN
R = 0.398 P = 0.23
Intercept = 2.8 Slope = -1
R = 0.757 P = 0.007
Intercept = 5.2 Slope = -1.5
R = 0.0483 P = 0.89
Intercept = 0.87 Slope = -0.09
Subcutaneous fat mass (g)
Epididymal fat mass (g)
Mesenteric fat mass (g)
1000 kcal

307

Figure 5. TXN decreases and alters the regional distribution of fat tissue accumulation. Mice were fed either a LFD (black, n = 12), a HFD (blue, n = 12), HFD+LXN (yellow, n = 12), HFD+HXN (red, n = 12), or HFD+TXN (green, n = 11) for 16 weeks. All fat masses were weighed on day of necropsy. (A) sWAT fat mass expressed as quartiles. (A-1) Relationship between sWAT fat mass and total caloric intake over 16 weeks of feeding for LFD; (A-2) HFD; (A-3) HFD+LXN; (A-4) HFD+HXN; and (A-5) HFD+TXN groups. (B) eWAT fat mass expressed as quartiles. (B-1) Relationship between eWAT fat mass and total caloric intake over 16 weeks of feeding for LFD; (B-2) HFD; (B-3) HFD+LXN; (B-4) HFD+HXN; and (B-5) HFD+TXN groups. (C) mWAT fat mass expressed as quartiles. (C-1) Relationship between mWAT fat mass and total caloric intake over 16 weeks of feeding for LFD; (C-2) HFD; (C-3) HFD+LXN; (C-4) HFD+HXN (with removal of two outliers); (C-5) and for HFD+TXN groups. Pre-planned general linear model with contrasts were used to calculate *p*-values in A, B and C. $*p < 0.05$, $**p < 0.01$, $***p < 0.001$. Linear regression analyses of total calories versus sWAT (A1-5), eWAT (B1-5), and mWAT fat masses (C1-5) in mice were done using stats package version 3.6.2 in R. Blue shading represents 95% CI of the regression line. Absolute value of R, p-value, intercept, and slope for the regression are reported above each corresponding panel. Source files of data used for the analysis are available in the Figure 5—source data 1.

Figure 5—source data 1

Source files.

This zip archive contains the following:

1) One Comma Separated Values file named “fig5_table.csv” phenotypic data directly pertaining to Fig. 5.
2) An R script file “ggplotRegression.R”.
3) A Jupyter Notebook file contains scripts used for statistical analysis and generation of Fig. 5.

333 **5. HXN and TXN protect against NAFLD on a high-fat diet**

334 NAFLD is characterized by accumulation of number and size of intrahepatic microvesicular and
335 macrovesicular lipid vacuoles. Mice on a LFD diet possessed hepatic lipid vacuoles and
336 resembled livers of $LDLR^{-/-}$ mice on a similar synthetic diet (Lytle and Jump, 2016); however
337 their liver to BW ratio of about 4% was in a normal healthy range (Lytle, Wong and Jump,
338 2017). HFD fed mice had many smaller lipid vacuoles (**Fig. 6A**). Supplementation with XN
339 decreased in a dose-dependent manner the number and size of intrahepatic lipid vacuoles in HFD
340 mice. Supplementation with TXN almost completely prevented hepatic lipid vacuole
341 accumulation in HFD mice, resulting in less lipid accumulation than in LFD mice.

342 The liver to BW ratio is an indicator of NAFLD with a ratio above 4% indicating
343 NAFLD (Lytle, Wong and Jump, 2017). The majority of mice (10 of 12) on a HFD diet had a
344 liver to BW ratio above 4.5%, whereas all LFD mice had a liver to BW ratio between 3.8 and
345 4.3% (**Fig. 6B**). Supplementation with HXN decreased the number of mice with a liver to BW
346 ratio above 4% to four of 12 mice and all TXN-supplemented mice had a liver to BW ratio below
347 3.6% except for one, which had a liver to BW ratio of 4%. These data are consistent with TXN
348 and, to a smaller extent, HXN reducing NAFLD. Hepatic lipid extracts from TXN-supplemented
349 HFD mice and LFD-fed mice had lower liver triglyceride concentrations than from mice fed with
350 HFD, LXN or HXN (**Fig. 6C**).

351 Another indicator of NAFLD is the liver area occupied by lipids; the histological lower
352 cut-off for NAFLD is over 5% of liver area (Brunt and Tiniakos, 2010). Using this cut-off, all
353 control HFD mice had NAFLD and 10 out of 12 LFD mice had NAFLD (**Fig. 3B**). Both HXN-
354 and TXN supplementation decreased liver lipid accumulation on a HFD by two-fold, as three out
355 of 12 HXN-supplemented mice and five out of 11 TXN-supplemented mice had less than 5%
356 lipid area and nine out of 11 TXN-supplemented mice had less than 10% lipid area (**Fig. 3B**). In
357 comparison, only one out of 12 HFD control mice and seven out of 12 HXN-supplemented mice
358 were below 10% lipid area. The supplement-induced decrease was independent of caloric intake
359 (**Fig 3. B3-5**).

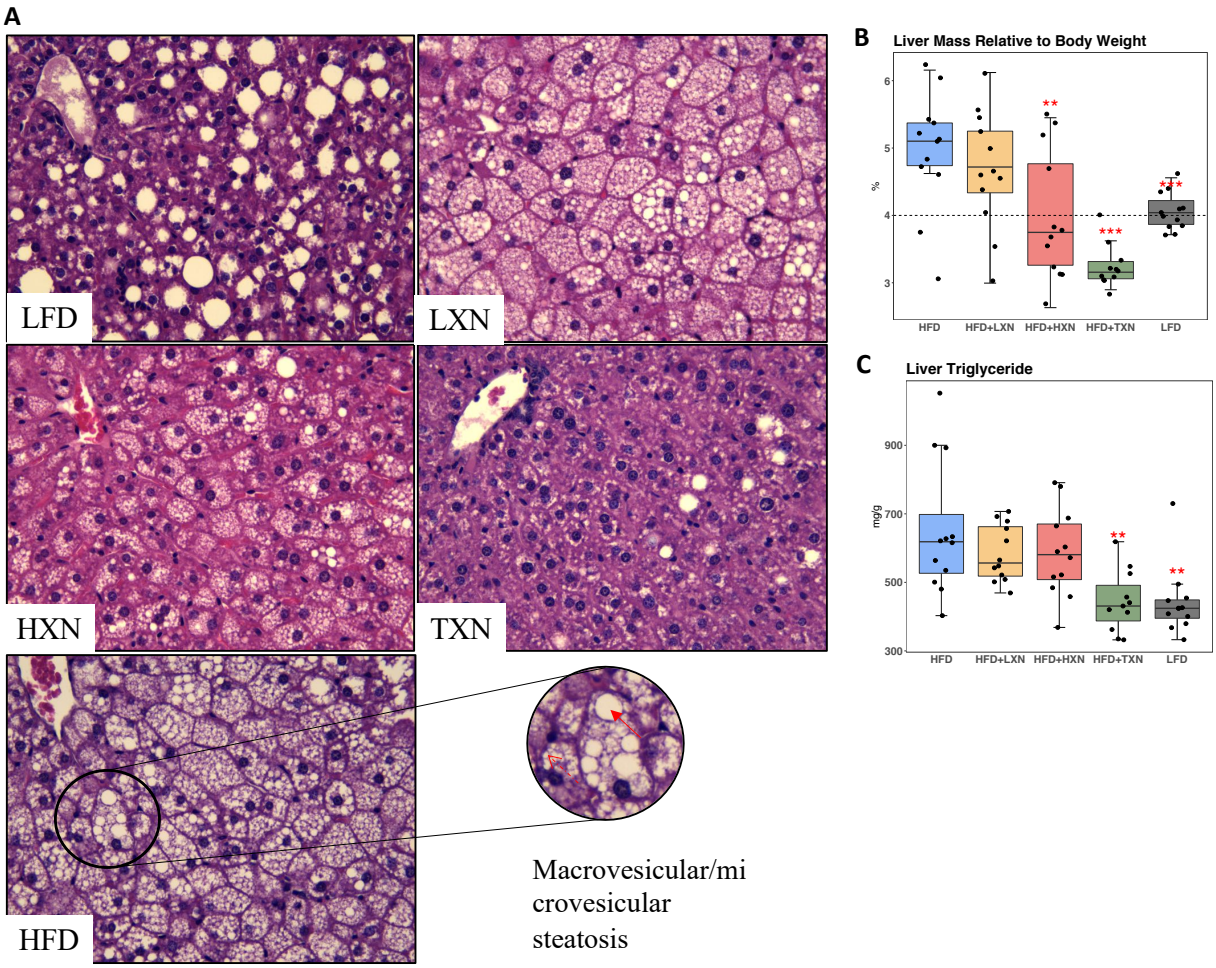

Figure 6. TXN prevents HFD induced liver steatosis in mice. Mice were sacrificed at the end of the study and liver samples were freshly collected and processed. (A) Representative histological images of H&E staining of liver sections. An enlarged image representative of a liver section from a HFD fed mouse is shown as a circle on the bottom right. Macrovesicular steatosis or large lipid droplets are indicated by the red bold arrow; microvesicular steatosis or small lipid droplets are indicated by the broken red line arrow. (B) Liver mass to BW ratio. (C) Hepatic triglyceride content. P-values of orthogonal *a priori* comparisons of the HFD versus each of the other groups are shown. $^{**}p < 0.01$, $^{***}p < 0.001$. Source files of data used for the analysis are available in the Figure 6—source data 1 and source data 2.

Figure 6-source data 1

Source files for histology data.

A folder called "TXN prevents HFD induced liver steatosis in mice" containing histology images in TIFF format (n = 59), used for histology scoring and Excel spreadsheet with scores and sample IDs. https://doi.org.

376 Figure 6-source data 2

377 This zip archive contains the following:

378 1) One Comma Separated Values file named “fig6_table.csv” phenotypic data directly pertaining to
379 Fig. 6.

380 2) A Jupyter Notebook file contains scripts used for statistical analysis and generation of Fig. 6

381 3) Two pdf files named “B.pdf” and “C.pdf”.

382 **5. RNA-seq reveals suppression of hepatic FA biosynthesis processes and pathways by**
383 **HXN and TXN treatments**

384 We conducted RNA-seq analysis of the livers obtained from mice after 16 weeks on the diet to
385 determine transcriptional mechanisms by which HXN and TXN supplementation could
386 ameliorate hepatic steatosis induced by HFD. Gene counts were calculated to quantify gene
387 expression in the four diet groups LFD, HFD, HFD+HXN, and HFD+TXN. The differentially
388 expressed genes (DEGs) were determined using a false discovery rate (FDR) cutoff of < 0.4, as
389 compared to HFD.

390 To visualize expression patterns of DEGs in the four groups we used hierarchical
391 clustering with a heat map (**Fig. 7A**). The DEGs clustered into two major types, one with higher
392 expression (red) in the LFD and HFD groups but lower expression (blue) in the HXN and TXN
393 groups and the other with lower expression in the LFD and HFD groups but higher expression in
394 the HXN and TXN groups (**Fig. 7A**). Individual mice clustered into two major nodes. All HFD
395 mice clustered with six LFD and four HXN mice and all TXN mice clustered with six HXN and
396 four LFD mice (**Fig. 7A**). This likely reflects the variability observed in phenotypic outcomes
397 (**Fig. 6 B**). The volcano plot analysis of gene expression revealed that both HXN and TXN
398 treatments induced significant changes in gene expression compared with the HFD group (**Fig.**
399 **7B**). TXN treatment had the greatest effect with 295 identified DEGs while HXN treatment only
400 resulted in six DEGs. We identified 212 DEGs in comparing the LFD and HFD groups.

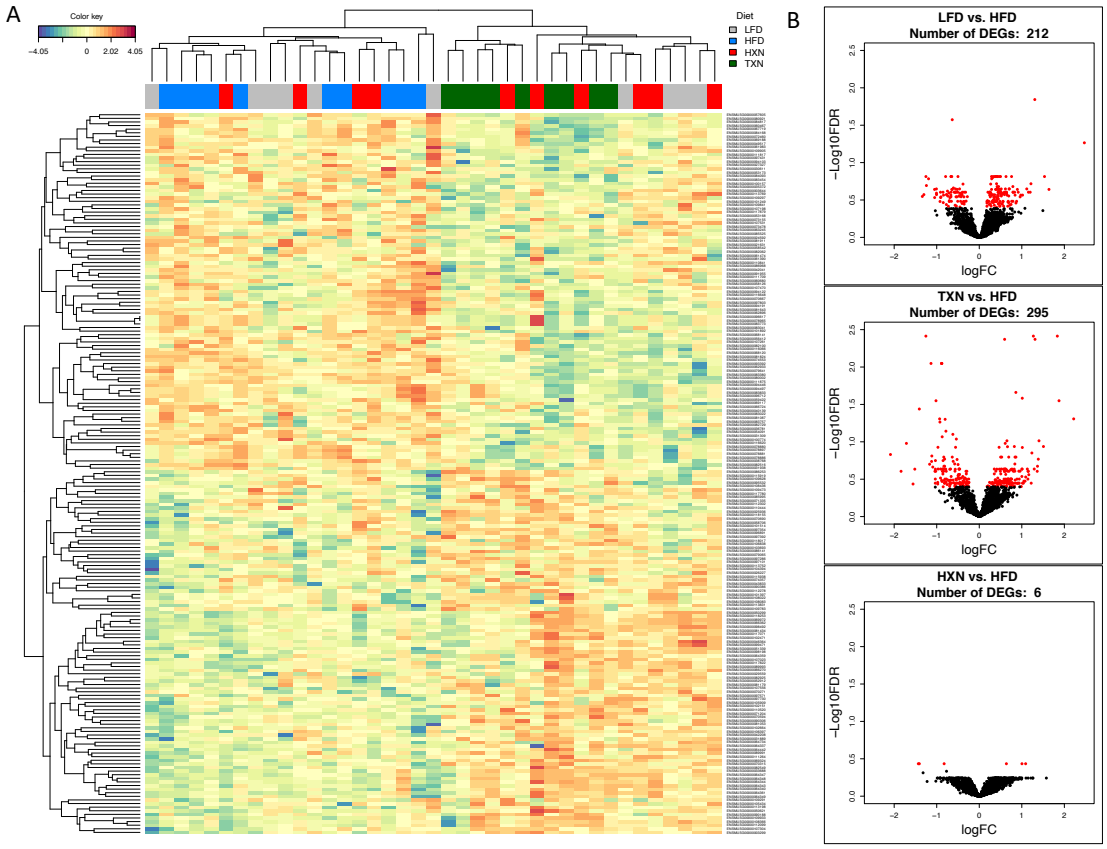

Figure 7. TXN treatment significantly alters liver transcriptome of mice after 16 weeks of feeding. (A) Hierarchical clustering of the top 200 differentially expressed genes (DEGs) in each treatment group (labeled at the top right corner: gray indicates LFD group, blue indicates HFD, red indicates HXN and green indicates TXN.) as determined by RNAseq analysis. Color key is based on the $\log_2$ fold change. (B) Volcano plots show DEGs (red dots) in the comparison of different treatment groups. Source files of data used for the analysis are available in the Figure 7—source data 1.

Figure 7—source data 1

Source files.

This zip archive contains the following:

1) A Jupyter Notebook file contains scripts used for statistical analysis and generation of Fig. 7.
2) A R object file in Rds format named “y_keep.rds”.
3) An R script used to generate the ‘y_keep.rds’ file.

415 We next conducted gene ontology (GO) enrichment and pathway analysis of DEGs using
416 Enrichr (Chen *et al.*, 2013). We assigned the DEGs in the TXN treatment group to GO terms
417 describing biological processes. The enriched GO terms and pathways with adjusted p values <
418 0.05 are summarized in **Figure 8 and Figure 8 source data**. GO enrichment analysis indicated
419 that TXN treatment significantly downregulated genes involved in biological processes including
420 xenobiotic catabolism, FA metabolism, glucose metabolism and regulation of lipid metabolism
421 (**Fig. 8,** top panel). Furthermore, KEGG pathway analysis demonstrated that TXN upregulated
422 expression of genes in six pathways including complement and coagulation cascades, prion
423 diseases, steroid hormone biosynthesis, arachidonic acid metabolism, retinol metabolism and
424 linoleic acid metabolism (**Fig. 8,** bottom right panel). Many of these included genes encoding
425 Cyp450 enzymes. On the other hand, expression of genes in 25 KEGG pathways were
426 significantly downregulated by TXN treatment compared to HFD (**Fig. 8,** bottom left panel). The
427 top 10 significantly enriched KEGG pathways based on statistical significance and combined
428 score ranking included the biosynthesis of unsaturated FAs, glutathione metabolism, amino sugar
429 and nucleotide sugar metabolism, glycolysis and gluconeogenesis, pentose phosphate pathway,
430 fluid shear stress and atherosclerosis, chemical carcinogenesis, drug metabolism, FA elongation
431 and the PPAR signaling pathway.

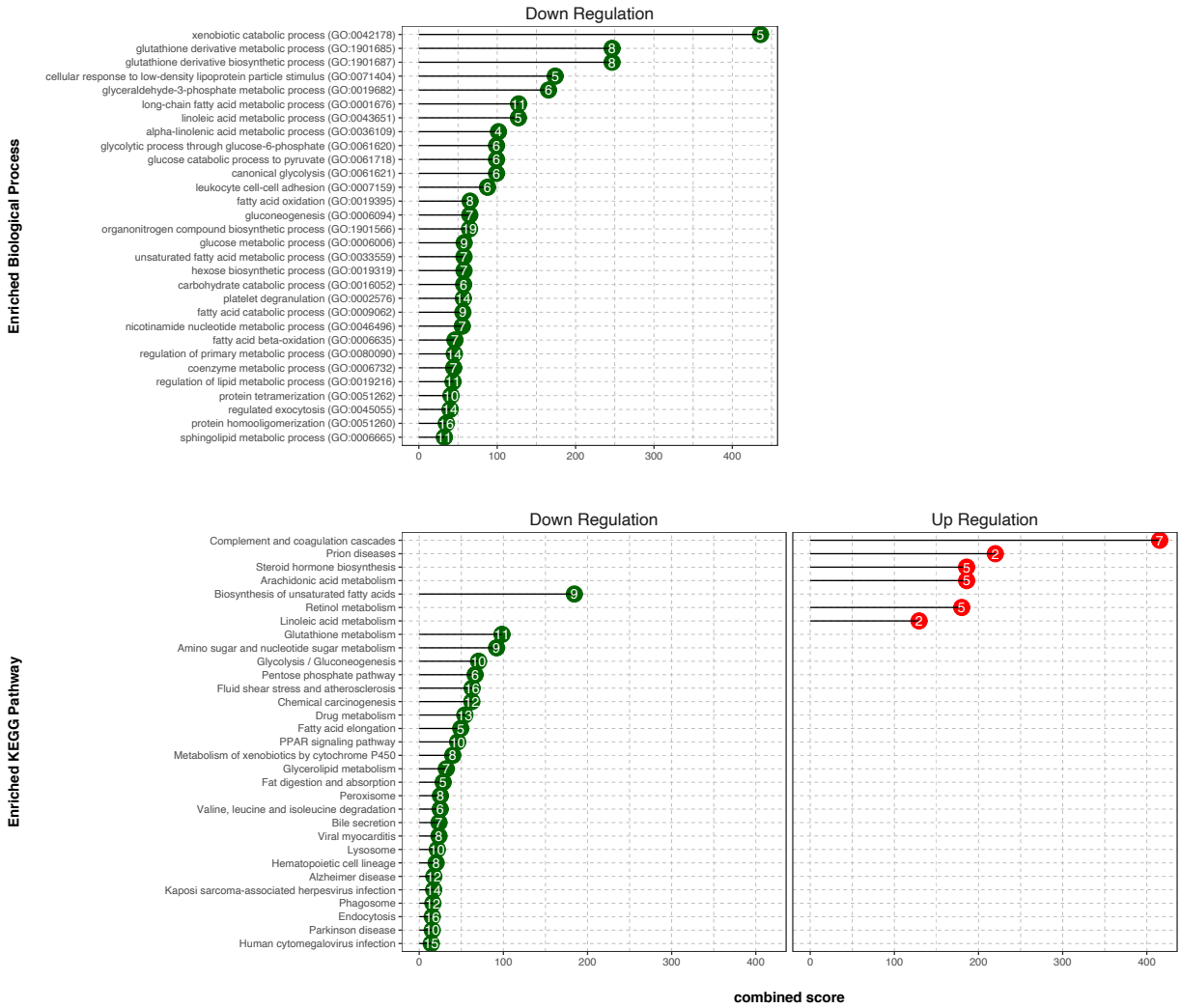

Figure 8. TXN decreases expression of numerous gene ontology and KEGG pathways. Analysis of DEGs from the livers of mice that consumed a HFD+TXN versus a HFD revealed mostly downregulation of biological processes and KEGG pathways. The significant (adjusted $p < 0.05$) enriched biological process terms in gene ontology (upper panel) and enriched KEGG pathways (lower panel) were selected by Enrichr Tools based on significance and combined scores. The number inside each lollipop represents the number of identified DEG genes in that specific biological process or KEGG pathway. Source files of data used for the analysis are available in the Figure 8—source data 1.

Figure 8—source data 1

Source files.

This zip archive contains the following:

1) A folder named “raw”, containing five Excel workbooks
    a. “DEGs_TXN_vs_HFD.xlsx”
    b. “DOWN-GO_Biological_Process_2018.xlsx”
    c. “UP-GO_Biological_Process_2018.xlsx”
    d. “DOWN-KEGG_2019_Mouse.xlsx”
    e. “UP-KEGG_2019_Mouse.xlsx”
2) A folder named “processed”, containing two Comma Separated Values files:
    a. “BPTerms.csv”
    b. “KEGGterms.csv”
3) A Jupyter Notebook file contains scripts used for statistical analysis and generation of Fig. 8.
4) A pdf file named “txnHFDGO.pdf”.

456 **6. Identification of key hepatic genes regulated by TXN and involved in ameliorating**
457 **hepatic steatosis**

458 We implemented SVM to identify a set of signature genes that can distinguish TXN-treated mice
459 from HFD-fed control mice. Briefly, we used the DaMirSeq R package to determine a set of
460 genes whose principal components best correlated with TXN treatment by performing backward
461 variable elimination with partial least-squares regression and removing redundant features by
462 eliminating those that were very highly correlated (Chiesa, Colombo and Piacentini, 2018).
463 Repeating this process 30 times, we used all 13 genes identified here as input into our SVM
464 models (**Fig. 9,** left panel). Genes identified classified HFD- and TXN-fed mice into two distinct
465 groups (**Fig. 9,** right panel). Eight of 13 genes showed significant, differential expression
466 between TXN and HFD diet samples (**Table 1**). Consistent with the GO analysis, three of the
467 eight genes – uncoupling protein 2 (*Ucp2*), cell death-inducing DFFA-like effector c (*Cidec*),
468 and monoacylglycerol O-acyltransferase 1 (*Mogat1*) – are involved in lipid metabolism and
469 known target genes of PPARγ (Medvedev *et al.*, 2001; Kim *et al.*, 2008; Matsusue *et al.*, 2008);
470 (Bugge *et al.*, 2010; Karbowska and Kochan, 2012; Wolf Greenstein *et al.*, 2017).

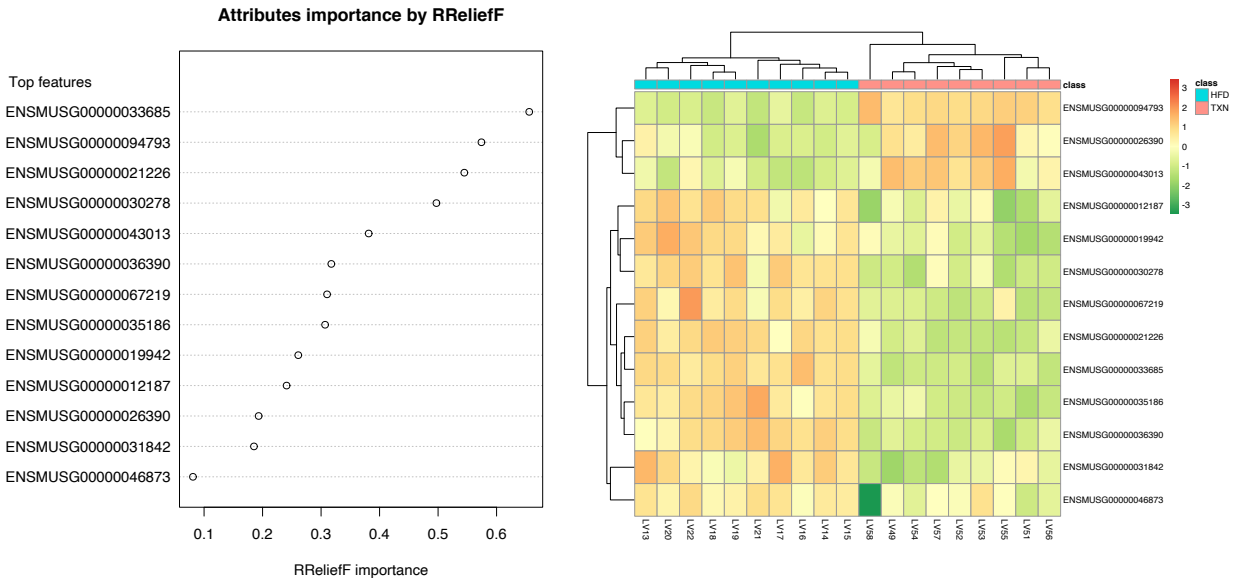

Figure 9. SVM identified signature genes that distinguish mice that consumed TXN. Left panel: the dot chart shows the top 13 genes, sorted by RReliefF importance score. This plot was used to select the most important predictors to be used for classification. Right panel: Colors in the heatmap highlight the gene expression level in fold change: color gradient ranges from *dark orange*, meaning "upregulated", to *dark green*, meaning "downregulated". On the top of the heatmap, horizontal bars indicate HFD (blue) and HFD+TXN (pink) treatments. On the top and on the left side of the heatmap the dendrograms obtained by Spearman's correlation metric are shown. Plots were produced with DaMiRseq R package 1.10.0. Source files of data used for the analysis are available in the Figure 9—source data 1.

Figure 9—source data 1

Source files.

This zip archive contains the following:

1) A Comma Separated Values file named "colData_hftxn.csv" contains experiment metadata.
2) A Comma Separated Values file named "countMatrix_hftxn.csv" contains raw counts in HFD and HFD+TXN groups.
3) A tab-delimited text file named "dfimportance_hftxn_lgcpm.txt".
4) A Jupyter Notebook file contains scripts used for statistical analysis and generation of Fig. 9.
5) A pdf file named "leftPanel.pdf".
6) A pdf file named "rightPanel.pdf".
7) A PowerPoint file named "fig9.pptx".
8) A pdf file named "fig9.pdf".

493 Table 1 Thirteen genes[a] used to distinguish TXN transcriptome from HFD transcriptome.

Ensemble ID	Gene name	Gene symbol	TXN vs. HFD (log_2 fold change)	P value	FDR
00000094793	major urinary protein 12	*Mup12*	2.65	***0.000***	0.011
00000033685	uncoupling protein 2	*Ucp2*	-1.07	***0.005***	0.109
00000036390	growth arrest and DNA-damage-inducible 45 alpha	*Gadd45α*	-0.73	0.083	0.402
00000021226	acyl-CoA thioesterase 2	*Acot2*	-1.33	***0.000***	0.003
00000030278	cell death-inducing DFFA-like effector c	*Cidec*	-2.41	***0.000***	0.006
00000043013	one cut domain, family member 1	*Onecut1*	1.53	***0.004***	0.098
00000067219	NIPA-like domain containing 1	*Nipal1*	-0.63	0.197	0.567
00000035186	ubiquitin D	*Ubd*	-2.51	***0.002***	0.068
00000031842	phosphodiesterase 4C, cAMP specific	*Pde4c*	-0.00	0.996	0.999
00000026390	macrophage receptor with collagenous structure	*Marco*	0.69	0.149	0.510
00000012187	monoacylglycerol O-acyltransferase 1	*Mogat1*	-1.62	***0.000***	0.011
00000019942	cyclin-dependent kinase 1	*Cdk1*	-1.53	***0.009***	0.139
00000046873	membrane-bound transcription factor peptidase	*Mbtps2*	-0.36	0.251	0.616

494 [a] Genes were ranked according to their *RReliefF* importance score using a multivariate filter technique
495 (*i.e., RReliefF*) (Chiesa et al., 2018). Also shown is the log_2 fold-changes, p values and FDR values when
496 HFD-TXN samples were compared with HFD samples using edgeR package (Robinson, McCarthy and
497 Smyth, 2010) in R. Negative values indicate genes down regulated in the liver with TXN
498 supplementation. Source files of data used for the analysis are available in the Table 1—source data 1.

499

500 Table 1—source data 1

501 Source files.

502 This zip archive contains the following:

503 1) An Excel workbook named "DEG_HFD_vs_TXN.xlsx" contains all differentially expressed
504 genes identified. Genes listed in the table were highlighted in yellow in the Excel workbook.

We then confirmed expression of these genes using RT-qPCR. Consistent with RNAseq results, TXN-treated mice had significantly lower expression of major PPARγ target genes *Cidec*, *Mogat1* and *Pparγ2,* a predicted PPAR target gene (Fang *et al.*, 2016) (**Fig. 10** top panel). Moreover, we observed significantly strong positive correlations between the expression of these three genes (**Fig. 10,** bottom panel). The above results suggest TXN treatment inhibits the PPARγ pathway – a key pathway involved in hepatic lipid metabolism.

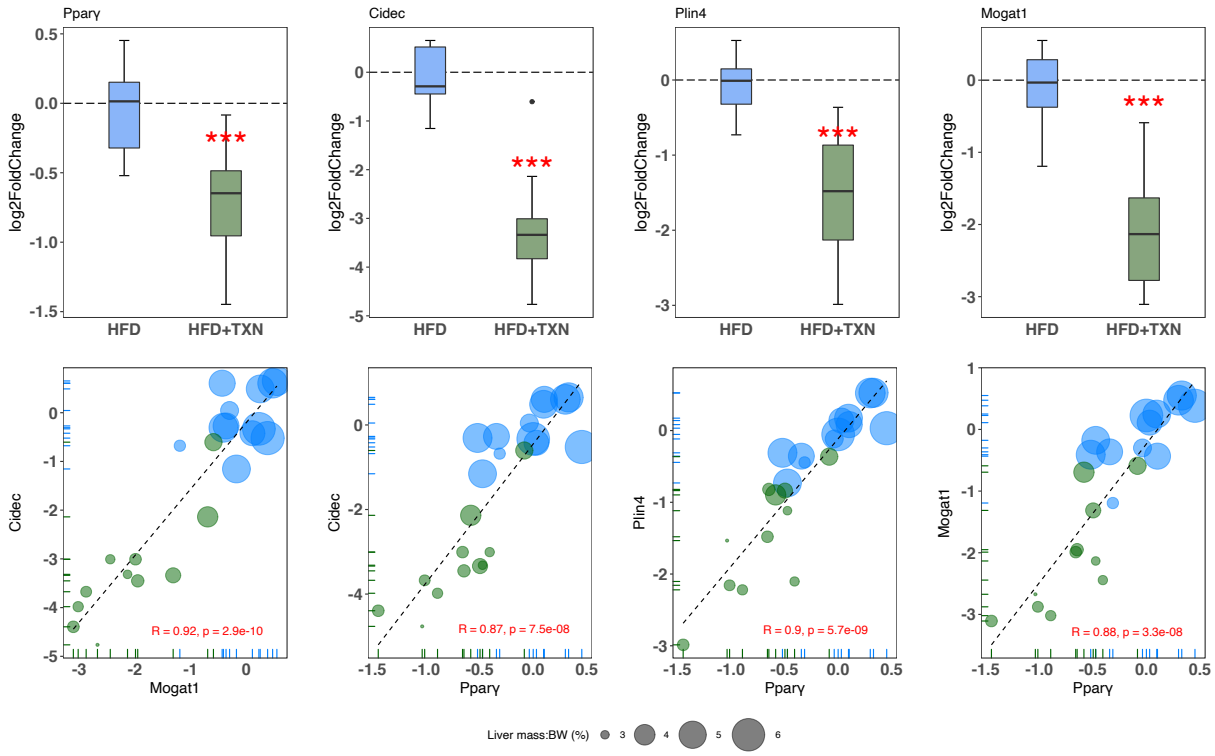

Figure 10. TXN-treated mice show significantly lower expression of PPARγ and target genes. Top panel: reduction of HFD-induced *Pparγ2*, *Cidec*, and *Mogat1* expressions in the liver by TXN administration. Mice were sacrificed after 16-week of HFD (blue, n = 12) or HFD+TXN (dark green, n = 11) feeding. Liver tissues were harvested, and total RNA was extracted. Relative mRNA levels of selected genes were determined by real time PCR. Gene expression is expressed in $\log_2$ fold change as quartiles. ***$p \leq 0.001$, t-test. Bottom panel: Pearson correlation between *Pparγ2* and *Cidec* or *Mogat1* expression. Data are presented in $\log_2$ fold change; bubble size represents liver mass to BW ratio. • indicates sample outside value, which is > 1.5 times the interquartile range beyond upper end of the box. Source files of data used for the analysis are available in the Figure 10—source data 1.

522 Figure 10—source data 1

523 Source files.

524 This zip archive contains the following:

525 1) A Comma Separated Values file named “fig10_table.csv” phenotypic data directly pertaining to
526 Fig. 10.
527 2) A Excel workbook named “PCR_lv_raw.xlsx” contains raw PCR cycle number data, and the
528 calculation of fold change.
529 3) A Jupyter Notebook file contains scripts used for statistical analysis and generation of Fig. 10.
530 4) A pdf file named “fig10.pdf”.

531 **7. XN and TXN attenuate intracellular lipid content in 3T3-L1 adipocytes in a dose**
532 **dependent manner**

533 We hypothesized that TXN and XN antagonizes the PPARγ receptor, which would explain the
534 decreased expression of its target genes. To test our hypothesis, we utilized 3T3-L1 murine
535 fibroblast cells, which depend on PPARγ activity to differentiate into adipocytes (Tamori *et al.*,
536 2002). XN and its derivatives are cytotoxic to some cells and to ensure that we used
537 concentrations that were not cytotoxic to 3T3-L1 adipocytes, we tested an escalating dose of XN
538 and TXN (Strathmann and Gerhauser, 2012). 3T3-L1 cells were treated with 0.1% DMSO, 1 μM
539 rosiglitazone (RGZ), 1 μM GW9662, XN (5, 10 and 25 μM), TXN (5, 10 and 25 μM), 25 μM
540 XN + 1 μM RGZ or 25 μM TXN + 1 μM RGZ for 48 h. After treatments, we determined the
541 number of live cells using an MTT assay. XN and TXN were only significantly cytotoxic for
542 3T3-L1 cells at a dose of 50 μM (data not shown). While it is difficult to translate *in vivo* doses
543 to *in vitro* doses, based on previous *in vitro* studies (Yang *et al.*, 2007; Samuels,
544 Shashidharamurthy and Rayalam, 2018) and our current cell viability data, we selected low (5
545 μM), medium (10 μM) and high (25 μM) concentrations of XN and TXN for the subsequent
546 experiments where cell viability was greater than 90% (data not shown).

547 Murine preadipocyte 3T3-L1 differentiation and adipogenesis was induced by addition of
548 dexamethasone, IBMX and insulin which strongly induced intracellular lipid accumulation (**Fig.**
549 **11, A2-3**). Addition of XN significantly attenuated intracellular lipid levels in a dose-dependent
550 manner (**B1-3**). Like XN, TXN also strongly inhibit intracellular lipid accumulation (**C1-3**).

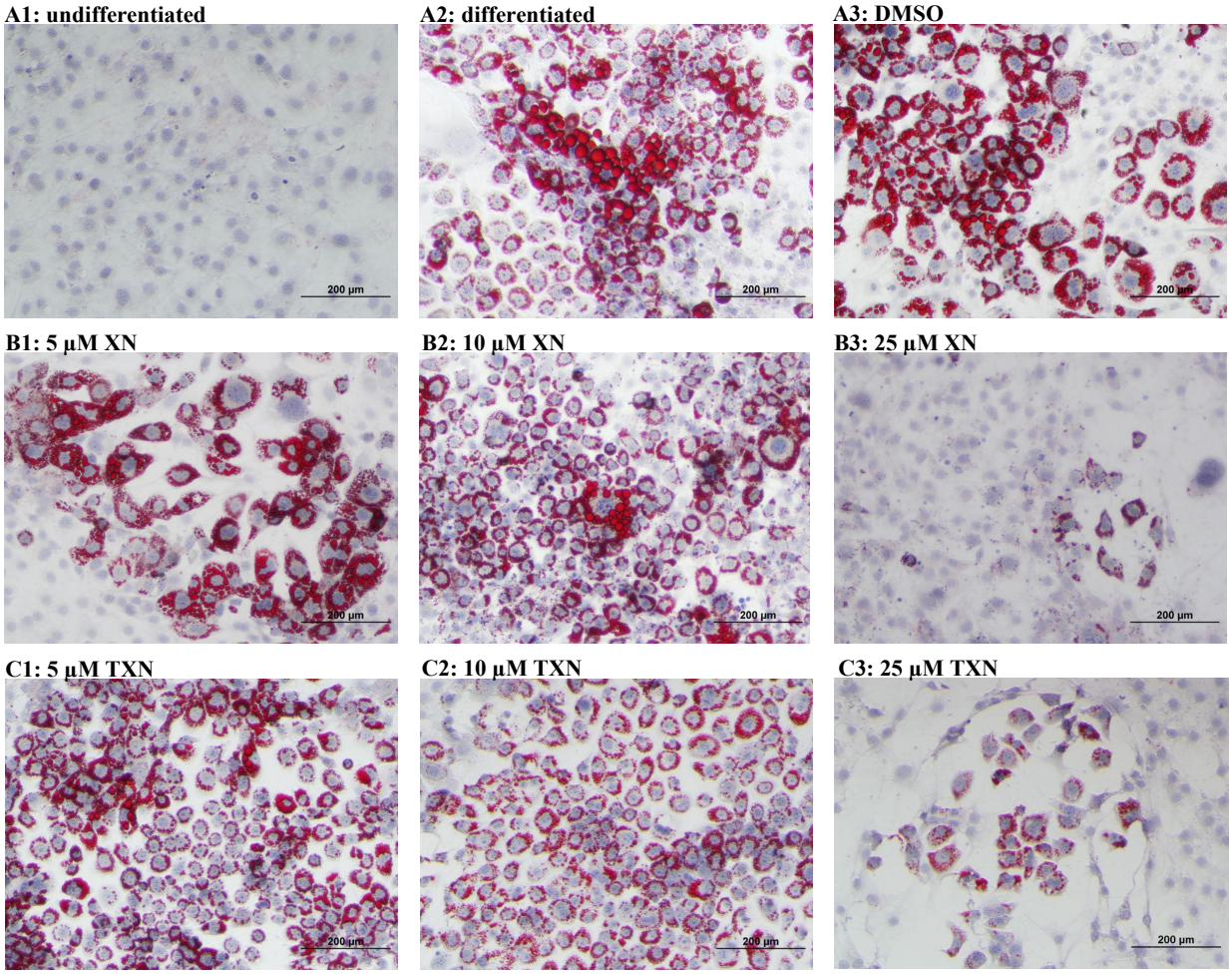

Figure 11. XN and TXN inhibit intracellular lipid accumulation in 3T3-L1 cells. 3T3-L1 cells ($1x10^6$ per well) in 12-well plates were cultured with either DMEM (A1), differentiation medium (DM) (A2), DM plus DMSO (A3), DM plus 5 µM XN (B1), DM plus 10 µM XN (B2), DM plus 25 µM XN (B3), DM plus 5 µM TXN (C1), DM plus 10 µM TXN (C2), or DM plus 25 µM TXN (C3). Cells were stained with oil red O to identify lipids at day 7 post-differentiation.

557 **8. XN and TXN inhibit RGZ-induced adipocyte differentiation in 3T3-L1 cells in a dose**
558 **dependent manner**

559 RGZ is a known potent PPARγ agonist used as an insulin-sensitizing agent. To test the
560 hypothesis that XN and TXN may antagonize a known PPARγ ligand, we determined if the
561 compounds would block RGZ-induced PPARγ actions (**Fig. 12**). RGZ strongly induced the
562 differentiation (**Fig. 12**, **A1**), and GW 9662, a potent PPARγ antagonist, inhibited the RGZ-
563 induced differentiation (**Fig. 12**, **A2**). We also observed that both XN (**Fig. 12**, **B1-3**) and TXN
564 (**Fig. 11**, **C1-3**) suppressed RGZ-induced differentiation in a dose dependent manner. At 25 μM
565 concentration, the RGZ-induced differentiation was largely blocked (**Fig. 12**, **B3, C3**),
566 suggesting that XN and TXN may interfere or even compete with binding of RGZ to the PPARγ
567 receptor.

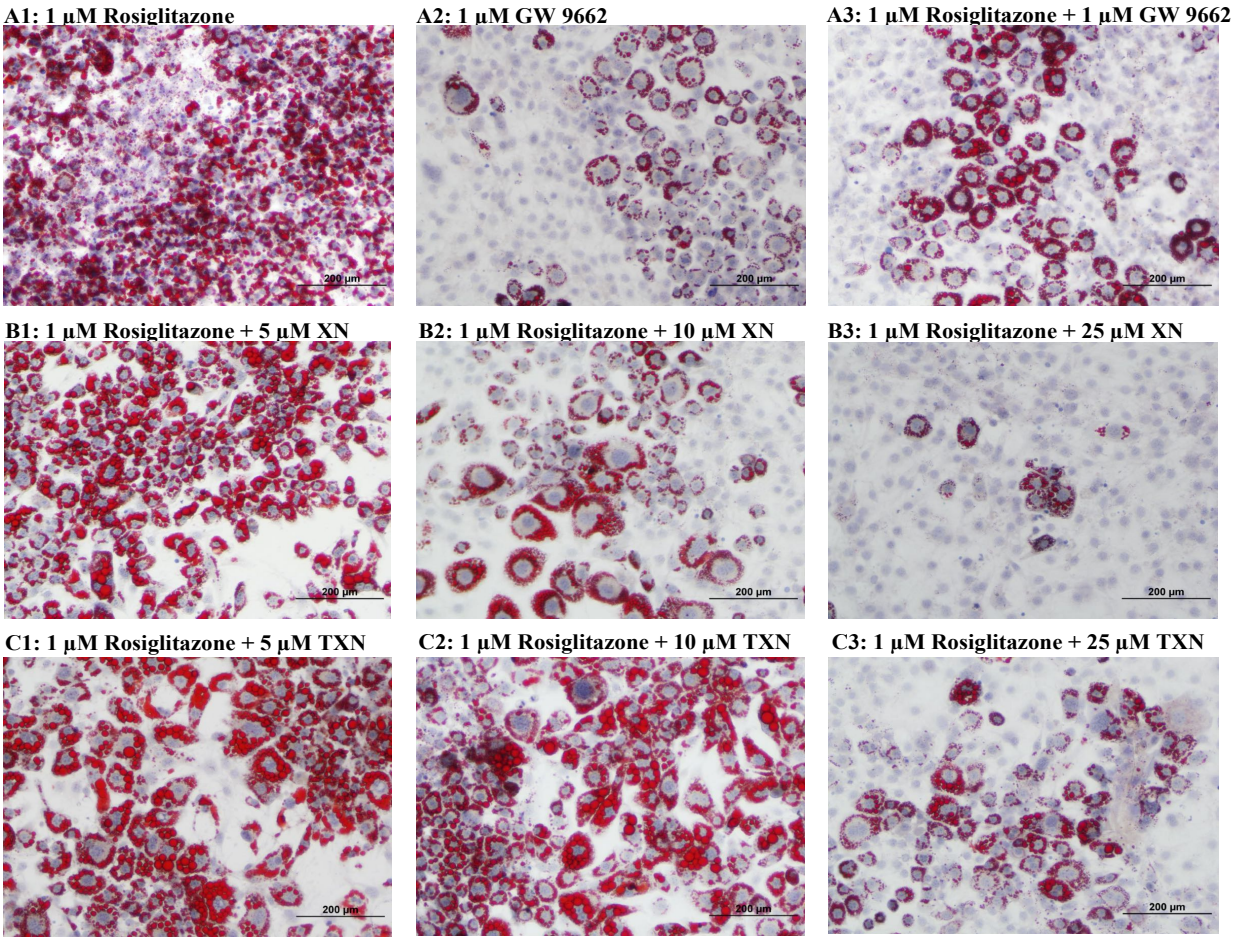

568

569 Figure 12. XN and TXN diminished the lipid accumulation in 3T3-L1 cells. 3T3-L1 cells ($1x10^6$ per well)
570 in 12-well plates were cultured with either DM plus 1μM rosiglitazone (A1), DM plus 1μM GW 9662
571 (A2), DM plus 1μM rosiglitazone and 1μM GW9662 (A3), DM plus 1 μM rosiglitazone and 5 μM XN
572 (B1), DM plus 1 μM rosiglitazone and 10 μM XN (B2), DM plus 1 μM rosiglitazone and 25 μM XN

573 (B3), DM plus 1 μM rosiglitazone and 5 μM TXN (C1), DM plus 1 μM rosiglitazone and 10 μM TXN
574 (C2), or DM plus 1 μM rosiglitazone and 25 μM TXN (C3). Cells were stained with oil red O to identify
575 lipids at day 7 post-differentiation.

576 **9. XN and TXN downregulate genes regulated by PPARγ in 3T3-L1 cells**

577 To elucidate the effect of XN and TXN on PPARγ action at the transcriptional level, we
578 measured the expression of several known PPARγ target genes using RT-qPCR on samples 7
579 days post 25 μM XN or TXN treatment. Consistent with the decrease of intracellular lipid
580 content in **Figures 10** and **11**, the expression of PPARγ and its target genes at 7 days post
581 treatment were significantly downregulated by XN and TXN treatments (**Table 2**). Cells treated
582 with 1 μM GW 9662, a PPARγ antagonist, did not significantly reverse the RGZ-induced
583 upregulation of these genes. Cells treated with either 25 μM XN or TXN significantly reversed
584 the RGZ-induced upregulation of *Cd36* ($p < 0.001$, $p < 0.001$), *Fabp4* ($p < 0.001$, $p < 0.001$),
585 *Mogat1* ($p < 0.001$, $p < 0.01$), *Cidec* ($p < 0.001$, $p < 0.001$), *Plin4* ($p < 0.001$, $p < 0.001$), *Fgf21*
586 ($p < 0.01$, $p < 0.01$). Taken together, these data above suggest that XN and TXN antagonize
587 PPARγ at the transcriptional level to block 3T3-L1 differentiation.

588 Table 2 Adipocyte gene expression at day 7 post-differentiation.

Gene	Log_2 (Fold Change)				p-values vs. RGZ		
	RGZ (cont)	RGZ + GW9662	RGZ + XN	RGZ + TXN	RGZ + GW9662	RGZ + XN	RGZ + TXN
Pparγ2	Ref.	-0.11	-1.93	-1.53	0.30	< 0.001	< 0.001
Cd36		-0.18	-9.10	-4.36	0.25	< 0.001	< 0.001
Fabp4		-0.12	-7.94	-4.08	0.43	< 0.001	< 0.001
Mogat1		-0.11	-4.16	-3.59	0.42	< 0.001	< 0.01
Cidec		-0.18	-10.10	-4.46	0.40	< 0.001	< 0.001
Plin4		-0.10	-3.01	-2.32	0.48	< 0.001	< 0.001
Fgf21		0.03	-0.99	-1.08	0.40	< 0.01	< 0.01

589 3T3-L1 differentiation was induced by IBMX, dexamethasone, insulin and 1 μM RGZ plus the addition
590 of 1 μM GW9662, 25 μM XN, or 25 μM TXN for 48 hours. After 48 hours, the old media was removed
591 and fresh DMEM was replenished for continuing differentiation. Gene expression was measured at day 7
592 post-differentiation using qRT-PCR. ΔCT = CT(target gene) – CT(reference gene). ΔΔCT = ΔCT(treated
593 sample) – ΔCT(untreated sample/control average). Fold change = $2^{-\Delta\Delta CT}$. Statistics were performed on
594 ΔΔCT values. Source files of data used for the analysis are available in the Table 2—source data 1.

595

596 Table 2—source data 1

597 Source files.

598 This zip archive contains the following:

599 2) An Excel workbook named “7days.xlsx” contains raw PCR cycle numbers, fold change,
600 log(2)fold change, p values, and how these are calculated.
601

602 **10. XN and TXN antagonize ligand binding to PPARγ**

603 Based on the inhibition of RGZ induced adipocyte differentiation, and expression of PPARγ
604 target genes, we postulated that XN and TXN bind to the PPARγ ligand binding domain and
605 interfere with agonist binding. To test this hypothesis, we first performed a competitive binding
606 assay using a PPARγ TR-FRET assay. Both XN and TXN displaced a labelled pan-PPARγ
607 ligand in a dose-dependent manner with IC_{50} values of 1.97 μM (**Fig. 13B**) and 1.38 μM (**Fig.**
608 **13C**), respectively. Oleic acid, the most abundant FA ligand in the HFD diet (**Table 4**), had an
609 IC_{50} value of 16.6 μM. XN and TXN had similar IC_{50} values as the PPARγ ligand PGZ, a drug
610 used to improve insulin sensitivity and type 2 diabetes, and a natural ligand, arachidonic acid
611 (Chen *et al.*, 2012).

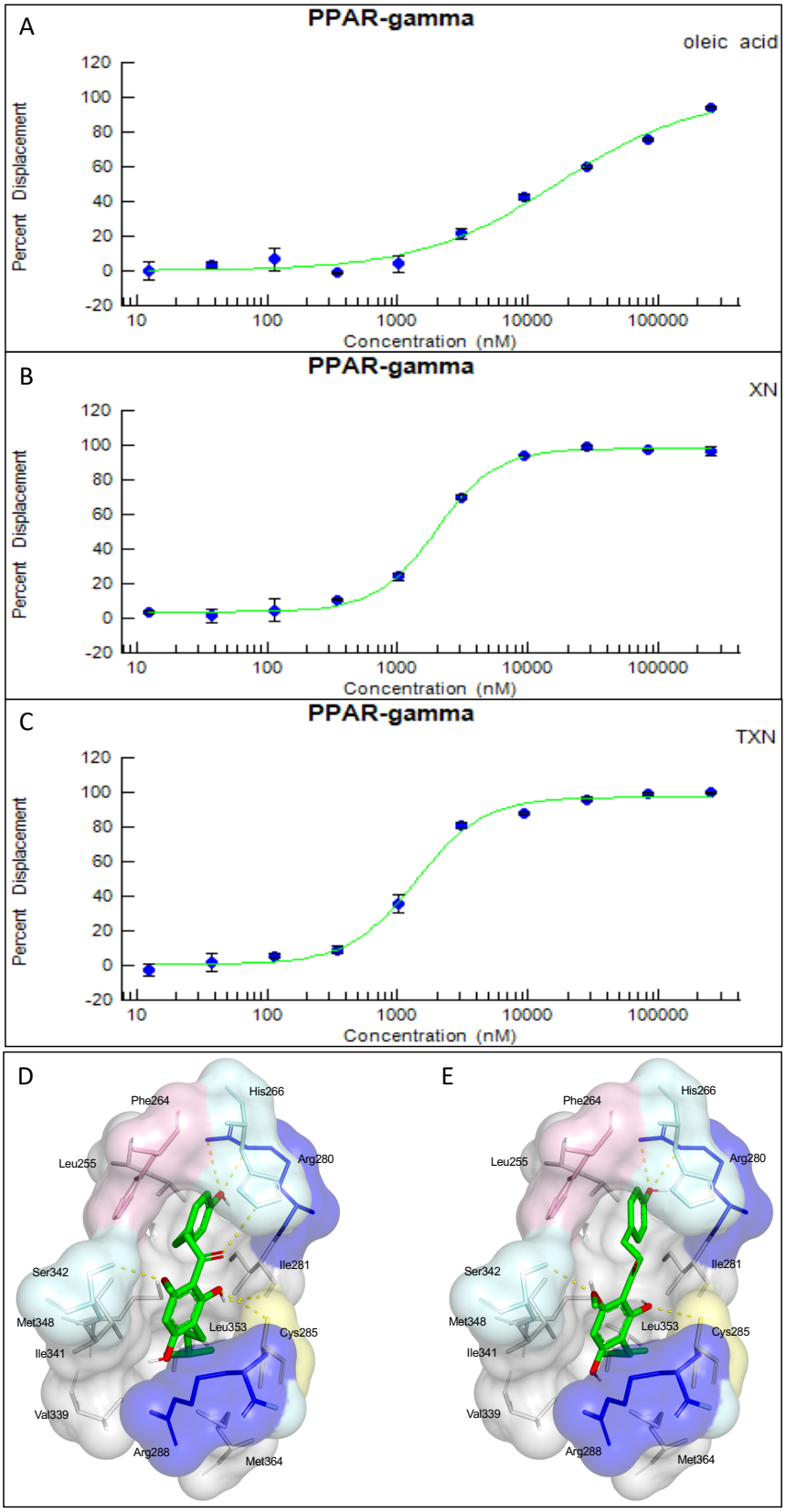
A
PPAR-gamma
oleic acid
Percent Displacement
Concentration (nM)
B
PPAR-gamma
XN
Percent Displacement
Concentration (nM)
C
PPAR-gamma
TXN
Percent Displacement
Concentration (nM)
D
E
Phe264
His266
Leu255
Arg280
Ser342
Ile281
Met348
Leu353
Cys285
Ile341
Val339
Arg288
Met364

612

613 Figure 13. XN and TXN are ligands for PPARγ. A PPARγ nuclear receptor competitive binding assay
614 based on time-resolved fluorescence resonance energy transfer (TR-FRET) was performed. The IC_{50}
615 values for each compound was determined by % displacement of a pan-PPARγ ligand. (A) Oleic acid IC_{50}
616 16.6 μM. (B) XN IC_{50} 1.97 μM. (C) TXN IC_{50} 1.38 μM. Molecular docking studies show TXN and XN
617 fit into the human PPARγ binding site. PPARγ residues containing atoms involved in hydrophobic
618 interactions are shown. Yellow dashes indicate hydrogen bonds, amino acids colored as hydrophobic
619 (grey), aromatic (pink), polar (cyan), basic (blue), or cysteine (yellow). (D) TXN (E) XN. Source files of
620 data used for the analysis are available in the Figure 13—source data 12.

621 Figure 13—source data 12

622 Source files: an Excel file named "SSBN12209_57828_10-point Titration_Inhibition_Results.xls"
623 containing results from ThermoFisher PPARγ nuclear receptor competitive binding assay.

624 To obtain further insights into the interaction of XN and TXN with PPARγ, we analyzed
625 the nature of binding between the PPARγ-LBD and XN/TXN using molecular docking to
626 confirm the putative binding pose and position of XN/TXN and to estimate the relative binding
627 affinities of various ligands for PPARγ. To verify the robustness of our docking protocol,
628 resveratrol was re-docked into the bound structure of PPARγ, reproducing the binding pose and
629 orientation found in the crystal structure of the complex (PDB ID: 4JAZ). The best docked
630 position of TXN occupies the binding site of PPARγ, exhibiting many non-bonded interactions
631 involving side chain atoms in Leu255, Phe264, Gly284, Cys 285, Arg288, Val339, Ile 341,
632 Met348, and Met364 (**Fig. 13 D**). The side chains of His266, Arg280, and Ser342 and the main
633 chain carbonyl oxygen atom of Ile281 are well positioned to make electrostatic/hydrogen bonds
634 with the hydroxyl protons and oxygen atoms of the bound TXN molecule. We observed many of
635 the same hydrophobic interactions in the simulated PPARγ-XN (**Fig. 13 E**) and PPARγ-oleic
636 acid complexes, and potential electrostatic interactions between His266 and Glu343, or with
637 Arg280 and XN or oleic acid, respectively. The relative binding affinities, ranked in decreasing
638 value of their negative binding energies were, in order, TXN, XN, and oleic acid, consistent with
639 the TR-FRET binding results.

640 ## Discussion

641 **XN and TXN are effective in suppressing development of diet-induced steatosis**

642 Low cost natural products like XN are of particular interest for treating obesity and NAFLD due
643 to their availability, safety and efficacy. XN and its derivatives appear to function through
644 multiple mechanisms of action and this polypharmacological effect may enhance their
645 effectiveness. Three studies propose that XN improves diet-induced hepatic steatosis by
646 suppressing SREBP1c mRNA expression and SREBP activation (Yui, Kiyofuji and Osada,
647 2014; Miyata *et al.*, 2015; Takahashi and Osada, 2017). We also observed a decrease in hepatic
648 SREPB1c expression with TXN treatment. Others propose mechanisms include inhibiting pro-
649 inflammatory gene expression (Dorn *et al.*, 2010; Mahli *et al.*, 2019), inducing AMPK activation
650 in the liver and skeletal muscle (Costa *et al.*, 2017), and enhanced FA oxidation (Kirkwood *et*
651 *al.*, 2013). In this study, using a combination of molecular, biochemical, biophysical and
652 bioinformatics approaches, we provide evidence for an additional novel mechanism by which
653 XN and its derivative, TXN, can inhibit diet-induced hepatic steatosis through downregulation of

654 hepatic FA uptake and lipid storage by binding to PPARγ in the liver and effectively
655 antagonizing its actions.
656 We previously demonstrated that XN and TXN ameliorated DIO in C57Bl6/J mice with
657 no evidence of liver injury (Miranda *et al.*, 2018). Using the same animal model, we confirmed
658 the phenotypic outcomes observed in the previous study (**Fig. 2**). In this study and prior studies
659 (Miranda *et al.*, 2018), we noted a decrease in weight with treatment in the presence of similar
660 caloric intake. Our metabolic cage data demonstrated energy expenditure increased with body
661 mass, but a treatment effect was not identified. We hypothesize that changes in microbiota
662 composition and bile acid metabolism which can affect nutrient and energy harvesting may
663 explain the reduction in weight (Wahlström *et al.*, 2016; Zhang *et al.*, 2020) observed by
664 treatment, but requires testing in future work. Furthermore, we demonstrated the effect of XN
665 and TXN on the development and progression of diet-induced hepatic steatosis. Administration
666 of XN (60 mg/kg BW) and TXN (30 mg/kg BW) significantly slowed the development and
667 progression of hepatic steatosis during a 16-week high fat feeding. We observed less macro- and
668 microvesicular steatosis, significantly lower liver mass to BW ratio, decreased TAG
669 accumulation, and significantly lower steatosis scores in the XN and TXN supplemented mice
670 compared to their untreated HFD mice (**Figs. 3B & 6**). Four pathways generally maintain hepatic
671 lipid homeostasis: uptake of circulating lipids, *de novo* lipogenesis (DNL), FA oxidation (FAO)
672 and lipid export in very low-density lipoproteins (VLDL). These pathways are under tight
673 regulation by hormones, nuclear receptors, and other transcription factors (Bechmann *et al.*,
674 2012). Long-term dysregulation of one and/or multiple processes can lead to the development of
675 NAFLD, obesity, type 2 diabetes and other metabolic disorders.
676 To elucidate the mechanism of XN and TXN, we determined liver transcriptomic
677 changes after 16 weeks of HFD feeding using RNAseq. We observed significant changes in
678 hepatic gene expression with TXN administration (**Fig. 7 B**). GO enrichment analysis of DEGs
679 revealed that several biological processes were significantly downregulated by TXN treatment,
680 including xenobiotic catabolism, FA metabolism, glucose metabolism and regulation of lipid
681 metabolism (**Fig. 8**). Furthermore, KEGG pathway analysis of DEGs revealed multiple
682 biological pathways were downregulated in the livers of TXN-treated mice, including
683 biosynthesis of unsaturated FAs, glutathione metabolism, amino sugar and nucleotide sugar
684 metabolism, glycolysis and gluconeogenesis, FA elongation, and PPAR signaling pathways,

685 suggesting that TXN rewired global hepatic lipid metabolism (**Fig. 8**). There was a paucity of
686 differentially expressed genes in the livers of mice supplemented with a high dose of XN (60
687 mg/kg BW) even at an FDR cutoff of 0.4. This discrepancy might be due to reduced levels of
688 XN in peripheral tissues as compared with TXN as we previously observed a 12-fold lower level
689 of XN as compared with TXN in the liver (Miranda *et al.*, 2018).
690 To discover signature genes in the liver of mice treated with TXN, we applied a SVM
691 classifier algorithm and extracted the most important features (genes) (**Fig. 9**). Due to the limited
692 number of samples in this study, we did not separate the data into training and testing sets for the
693 construction of SVM. The caveat of this is that the learning model might not generalize well.
694 Consistent with GO analysis, three out of the eight significantly regulated genes – uncoupling
695 protein 2 (*Ucp2*), cell death-inducing DFFA-like effector c (*Cidec*), and monoacylglycerol O-
696 acyltransferase 1 (*Mogat1*) – are involved in lipid metabolism **(Table 1)**. Notably, these genes
697 are targets of PPARγ (Bugge *et al.*, 2010; Karbowska and Kochan, 2012; Wolf Greenstein *et al.*,
698 2017). PCR confirmed this finding (**Fig. 10**) and suggests that TXN modulates PPARγ actions.

699 **XN and TXN are novel natural and synthetic PPARγ antagonists**

700 PPARγ belongs to a superfamily of nuclear receptors and just like other members, its
701 activity requires ligand binding. PPARγ is highly expressed in white and brown adipose tissue,
702 and to a lesser extent in the liver, kidney, and heart (Zhu *et al.*, 1993; Lee and Ge, 2014).
703 Because of its essential role in regulating adipogenesis and higher expression in the white
704 adipose tissue, PPARγ has been a pharmacological target for drug development (Lehmann *et al.*,
705 1995; Lefterova *et al.*, 2014) in combating metabolic diseases such as insulin resistance and type
706 2 diabetes. Thiazolidinediones (TZDs), which include RGZ and PGZ, are the most widely
707 investigated PPARγ agonists due to their strong insulin-sensitizing ability (Henney, 2000;
708 Soccio, Chen and Lazar, 2014). Studies show that the main action of TZDs occurs in adipocytes
709 (Chao *et al.*, 2000). In the liver, PPARγ plays a role in hepatic lipogenesis (Sharma and Staels,
710 2007). Multiple clinical trials using TZDs have observed significant improvement in hepatic
711 steatosis and inflammation (Ratziu *et al.*, 2008, 2010; Sanyal *et al.*, 2010), suggesting additional
712 actions of TZDs in non-adipocytes. Interestingly, PGZ is more effective in treating fatty liver
713 disease than RGZ, the more potent PPARγ agonist (Promrat *et al.*, 2004; Ratziu *et al.*, 2008,
714 2010), suggesting moderate binding is more effective. Unfortunate side effects of TZDs are
715 weight gain (Fonseca, 2003), bone loss (Schwartz and Sellmeyer, 2007; Schwartz, 2008), edema

716 and increased risk of cardiovascular complications (Nesto *et al.*, 2004; Yang and Soodvilai,
717 2008; Bełtowski, Rachańczyk and Włodarczyk, 2013), due to over-activation of PPARγ. Thus,
718 there is great interest in identifying "ideal" PPARγ modulators that are tissue specific with
719 limited side effects.

720 An alternative strategy that aims to repress PPARγ has emerged in recent years
721 (Ammazzalorso and Amoroso, 2019). The potential of reducing BW and improving insulin
722 sensitivity suggests a possible clinical role of PPARγ antagonists in treating obesity and type 2
723 diabetes (Yamauchi *et al.*, 2001; Rieusset *et al.*, 2002; Nakano *et al.*, 2006). Compared to
724 agonists, researchers have identified only a few natural compounds that inhibit PPARγ, all of
725 which have a moderate binding affinity for PPARγ receptor and can inhibit adipogenesis, obesity
726 and/or hepatic steatosis. These include resveratrol (Calleri *et al*., 2014), 7-chloroarctinone-b
727 isolated from the roots of *Rhaponticum uniflorum* (Li *et al.*, 2009), tanshinone IIA from the roots
728 of *Salvia miltiorrhiza* (danshen) (Gong *et al.*, 2009), astaxanthin from red-colored aquatic
729 organisms (Jia *et al.*, 2012), protopanaxatriol (PPT) extracted from *Panax ginseng* roots (Zhang
730 *et al.*, 2014), foenumoside B from the herbal plant *Lysimachia foenum-graecum* (Kwak *et al.*,
731 2016), and betulinic acid, a pentacyclic triterpene found in the bark of several plants (Brusotti *et*
732 *al.*, 2017; Ammazzalorso and Amoroso, 2019).

733 Several lines of evidence presented in this study support the hypothesis that XN and TXN
734 are also PPARγ antagonists. First, using the 3T3-L1 cell model for PPARγ-mediated
735 adipogenesis, we demonstrated that XN and TXN significantly and strongly suppressed RGZ
736 induced adipocyte differentiation and adipogenesis by day 7 (**Fig. 12**). Consistent with a
737 decrease in lipid accumulation, PPARγ target genes were also significantly downregulated in XN
738 and TXN-treated cells (**Table 2**). The PPARγ antagonist, GW9662, did not significantly affect
739 target gene expression of PPARγ, even though it inhibited differentiation (**Fig.12 A2-3**). In our
740 experiments, we used a significantly lower concentration of GW9662 than used by others that
741 ranged from 3-25 times higher, and this difference could explain our results (Park *et al.*, 2008;
742 Kim, Nian and McIntosh, 2011; Sankella, Garg and Agarwal, 2016). Second, the PPARγ nuclear
743 receptor competitive binding assay showed that XN and TXN have a moderate binding affinity
744 of 1.97 μM and 1.38 μM, respectively (**Fig. 13**). Lastly, consistent with the competitive binding
745 assay, simulated molecular docking indicated that XN and TXN can interact with the ligand
746 binding domain of PPARγ like other known ligands and potentially form hydrogen bonds with

747 His266, Arg280, Ser342 and Ile281, in addition to many non-bonded interactions (**Fig. 13 D,E**).
748 Moreover, the predicted binding model reveals that the interactions between XN, TXN and the
749 PPARγ ligand binding domain resembles those observed between PPARγ and resveratrol, a
750 dietary polyphenol that is also a PPARγ antagonist (Calleri *et al.*, 2014). Our findings are
751 consistent with XN and TXN functioning as PPARγ antagonists and now offer a mechanistic
752 explanation for prior observations that XN impaired adipocyte differentiation (Yang et al., 2007;
753 Mendes et al., 2008; Samuels, Shashidharamurthy and Rayalam, 2018).
754 One of the many side effects observed from TZD therapy is weight gain. TZDs primarily
755 mediate their effects in adipose tissue by PPARγ activation that stimulates adipocyte
756 differentiation and increases the efficiency of uptake of circulating non-esterified FAs (NEFA)
757 by adipocytes (Rosen and Spiegelman, 2006). Interestingly, in this study, we observed a
758 significant decrease in overall, sWAT, and mWAT fat mass in HXN- and TXN-treated mice
759 (**Figs. 3A, 5AC**), yet a slight increase in the eWAT fat mass (**Fig. 5B**). Prior studies have
760 reported that the expandability of eWAT in male mice is an indicator of metabolic health. Mouse
761 sWAT and mWAT will continue to expand with BW, whereas eWAT expansion diminishes after
762 mouse BW reaches about 40 g (van Beek *et al.*, 2015). Our data suggest that HXN- and TXN-
763 treated mice have capacity to expand eWAT, whereas HFD-fed untreated mice do not, which
764 seems to direct the development of metabolic disorders. In our previous study, we demonstrated
765 that XN and TXN accumulates primarily in the liver with significantly lower levels in the muscle
766 (Miranda *et al.*, 2018). We could not detect XN or TXN in the WAT of these mice (data not
767 shown). The levels of XN and TXN in the liver (TXN > HXN > LXN) and the absence of both
768 compounds in the WAT suggests that these compounds antagonize PPARγ in the liver and not in
769 the WAT, therefore, minimizing the side effect of weight gain observed with TZDs that are
770 PPARγ agonists.
771 During a long term HFD feeding, PPARγ and its target genes are upregulated to
772 compensate for the lipid overflow in the liver. Namely, genes associated with lipid uptake and
773 trafficking (*Lpl*, *Cd36*, *Fabp4*), TAG synthesis (*Fasn*, *Scd1*, *Mogat1*), and formation of lipid
774 droplets for storage (*Cidec*/*Fsp27*, *Plin4*) (Supplement_File_B). The result is excessive lipid
775 accumulation in the liver, leading to hepatic steatosis. This was observed with PPARγ
776 overexpression in hepatocytes in *ob/ob* mice (Wolf Greenstein *et al.*, 2017). We propose that
777 TXN added to a HFD antagonizes PPARγ action in the liver potentially by physically interacting

778 with PPARγ receptors as indicated in the molecular docking studies (**Fig. 13 DE**) and; therefore,
779 reduces PPARγ transcriptional activity and expression of the aforementioned target genes.
780 Several *in vivo* studies support our findings. Liver-specific PPARγ deficiency protects *ob/ob*
781 mice from hepatic steatosis (Matsusue *et al.*, 2003); knockdown of *Mogat1* in the liver
782 significantly attenuates hepatic steatosis after 12 weeks HFD feeding (Lee *et al.*, 2012); and
783 restoration of CIDEC/FSP27 in *ob/ob* liver-specific PPARγ knockout mice promotes hepatic
784 steatosis (Matsusue *et al.*, 2008). The role for PLIN4 in hepatic steatosis is limited, but it may
785 affect TAG accumulation during HFD feeding (Griffin *et al.*, 2017).
786 In conclusion, we demonstrated that TXN is very effective in suppressing the
787 development and progression of diet induced hepatic steatosis in mice. TXN appears more
788 effective in-vivo than XN perhaps due to significantly higher levels of TXN in the liver, but XN
789 can slow progression of the condition at a higher dose. We provide evidence that XN and TXN
790 act as novel, natural and synthetic antagonists of PPARγ that bind with a similar affinity as the
791 agonist PGZ. Our findings support further development of XN and TXN as novel, low-cost
792 therapeutic compounds for diet-linked hepatic steatosis with fewer negative side effects than
793 current drugs (e.g., reduced adipose tissue expansion). Additionally, the structures of XN and
794 TXN could serve as scaffolds for the synthesis of more effective compounds to treat NAFLD and
795 other fatty liver diseases. Although these results are encouraging, further studies are required to
796 clarify possible use in humans for the prevention and treatment of diet-linked hepatic steatosis.

797 Materials and Methods

798 Animals and diets

799 Studies were performed using 8-week-old SPF male C57BL/6J mice obtained from The Jackson
800 Laboratory (Bar Harbor, ME, USA). Upon arrival, 60 mice were housed individually in
801 ventilated cages in a controlled environment (23 ± 1ºC, 50-60% relative humidity, 12 hours
802 daylight cycle, lights off at 18:25 hours) with food and water *ad libitum*. After acclimating mice
803 for one week on a normal-chow diet (PicoLab Rodent Diet 20, 5053, TX, USA) followed by
804 two-weeks on a low-fat control diet (LFD, Dyets Inc., Bethlehem, PA, USA), they were
805 randomly assigned (restricted) to five groups (n = 12/group). The sample size of 12 mice per
806 treatment group was based on previous published studies (Miranda *et al.*, 2016, 2018). The
807 groups were fed either a LFD, HFD, HFD + 30 mg/kg BW/day XN (LXN), HFD + 60 mg/kg

808 BW/day XN (HXN), or HFD + 30 mg/kg BW/day TXN (TXN). The sources and purity of XN
809 and TXN were described previously (Miranda *et al.*, 2018). The chemical structures of XN and
810 TXN, a detailed diet composition and FA composition are available in **Figure 1**, **Table 3** and
811 **Table 4**, respectively.

812 Table 3 Composition of diets[a]

	HFD	HFD+LXN	HFD+HXN	HFD + TXN	LFD
Ingredient (g/100g)					
Casein	2.58	2.58	2.58	2.58	1.89
L-Cystine	0.04	0.04	0.04	0.04	0.03
Sucrose	0.89	0.89	0.89	0.89	0.89
Cornstarch	0.00	0.00	0.00	0.00	4.02
Cellulose	0.54	0.54	0.54	0.54	0.47
Dyetrose	1.62	1.62	1.62	1.62	1.62
Soybean Oil	0.32	0.32	0.32	0.32	0.24
Lard	3.17	3.17	3.17	3.17	0.19
Mineral Mix #210088	0.13	0.13	0.13	0.13	0.10
Dicalcium Phosphate	0.17	0.17	0.17	0.17	0.12
Calcium Carbonate	0.07	0.07	0.07	0.07	0.05
Potassium Citrate H_2O	0.21	0.21	0.21	0.21	0.16
Vitamin Mix #300050	0.13	0.13	0.13	0.13	0.10
Choline Bitartrate	0.03	0.03	0.03	0.03	0.02
Test compound	0.00	0.003	0.006	0.003	0.00
OPT	0.10	0.10	0.10	0.10	0.10
Composition (kcal%)					
Protein	20	20	20	20	20
Carbohydrates	20	20	20	20	70
Lipids	60	60	60	60	10
Energy Density (kcal/g)	5.12	5.12	5.12	5.12	3.55

813 [a]LXN provides 30 mg/kg BW xanthohumol (XN), HXN 60 mg/kg XN, and TXN 30 mg/kg Tetrahydro-
814 XN (TXN) per day. The test compounds were dissolved in an isotropic mixture of oleic acid: propylene
815 glycol: Tween 80 (OPT) 0.9:1:1 by weight before incorporation into the diets. All diets were purchased
816 from Dyets Inc., Bethlehem, PA, USA.

817 Table 4 Fatty acid composition (% of the total fat) of the low-fat diet (LFD) and high-fat diet (HFD).

Fatty Acids	**% of the total fat**		**g/kg diet**	
	LFD	HFD	LFD	HFD
14:0 Myristic	0.7	1.4	0.29	4.75
16:0 Palmitic	17.0	24.2	7.28	84.34
16:1 Palmitoleic	1.5	3.1	0.65	10.76
18:0 Stearic	8.3	12.3	3.56	42.92
18:1 Oleic	32.2	42.1	13.76	146.95
18:2 Linoleic	35.2	14.9	15.04	51.89
18:3 Linolenic	5.0	2.1	2.14	7.27
SFAs	26.0	37.9	11.13	132.01
MUFAs	33.7	45.2	14.41	157.71
PUFAs	40.2	17.0	17.18	59.16
Total n-6 PUFA	35.2	14.9	15.04	51.89
Total n-3 PUFA	5.0	2.1	2.14	7.27

818 Abbreviations: SFA: saturated fatty acids; MUFAs: monounsaturated fatty acids; PUFAs:
819 polyunsaturated fatty acids; n-6: omega-6 fatty acids; n-3: omega-3 fatty acids.

820 BW gain and food intake of individual mice were assessed once per week. Body
821 composition was determined at the end of the feeding using a Lunar PIXImus 2 Dual Energy X-
822 ray Absorptiometer (DXA) scan (Madison, WI, USA). After 16 weeks of feeding the control and
823 test diets, mice were fasted for 6 h during the dark cycle, anaesthetized in chambers saturated
824 with isoflurane and then euthanized by cardiac puncture followed with cervical dislocation.
825 Blood was collected in syringes containing 2 IU of heparin and centrifuged to separate plasma
826 from cells. The liver and sWAT, mWAT, and eWAT fat pads were carefully collected and
827 weighed. To avoid batch effect due to difference in hours of fasting, mice were randomized
828 (restricted) and treatment information was masked before sacrifice. The Institutional Animal
829 Care and Use Committee (IACUC) at Oregon State University approved all animal work (ACUP
830 5053). All animal experiments were performed in accordance with the relevant guidelines and
831 regulations as outlined in the Guide for the Care and Use of Laboratory Animals.

832 **Liver histology**

833 Liver (~100 mg) was freshly collected from mice and immediately fixed overnight in 10%
834 neutrally buffered formalin, paraffin embedded, sectioned, and stained with hematoxylin-eosin
835 (Veterinary Diagnostic Laboratory, Oregon State University, OR). Each slide contained two liver
836 sections that were examined using a Leica microscope at 100× magnification. Representative
837 images were taken at 100× magnification from the subjectively least and most severely affected

838 areas ensuring representation of all zones of the hepatic lobule. Steatosis was objectively
839 quantified as percent surface area occupied by lipid vacuoles using ImageJ for image analysis
840 (NIH; imagej.nih.gov/ij/index.html) as previously published (Garcia-Jaramillo *et al.*, 2019).

841 **Energy expenditure**

842 Indirect calorimetry measurements were based on an open respirometer system. From week 10,
843 mice were housed individually in Promethion® Line metabolic phenotyping chambers (Sable
844 Systems International, Las Vegas, NV, USA) and maintained on a standard 12 h light/dark cycle
845 for three days. The system consisted of 10 metabolic cages, each equipped with food and water
846 hoppers connected to inverted laboratory balances for food intake monitoring; both food and
847 water were available *ad-libitum*. Spontaneous physical activity (SPA) was quantified via infrared
848 beam breaks in X and Y axes, and included locomotion, rearing, and grooming behaviors (BXY-
849 R, Sable Systems International). All raw data from all sensors and analyzers were stored every
850 second. Air within the cages was sampled through micro-perforated stainless-steel sampling
851 tubes located around the bottom of the cages, above the bedding. Ambient air was passed
852 through the cages (2 L/min) and gases were sampled continuously for each cage, allowing the
853 simultaneous acquisition of metabolic data every second, for all cages in the system (Lighton and
854 Halsey, 2011). The energy expenditure was estimated from oxygen consumption (VO_2) and
855 carbon dioxide production (VCO_2) rates by the Promethion system using the Weir formula
856 (Weir, 1949).

857 **Liver tissue RNA extraction and library preparation**

858 Freshly dissected liver tissue was flash frozen in liquid N_2 and then stored at -80ºC. Total RNA
859 was isolated using the Direct-zol RNA Miniprep Plus kit as instructed (Zymo Research, Irvine,
860 CA, USA). RNA concentrations were quantified using the Qubit™ 1.0 Fluorometer and the
861 Qubit RNA BR Assay kit (Thermo Fisher Scientific, Waltham, MA, USA). RNA purity and
862 integrity were evaluated using a Bioanalyzer RNA 6000 Nano chip (Agilent Technologies, Santa
863 Clara, CA, USA). Samples ranged from medium to high RNA quality (RIN 5.9-8.3), and
864 samples with different RIN values showed similar RNA-seq qualities.

865 Each library was prepared with 325 ng total RNA using the Lexogen QuantSeq 3'mRNA-
866 Seq Library Prep Kit-FWD for Illumina sequencing according to the manufacturer's instructions
867 (Lexogen GmbH, Vienna, Austria). Briefly, library preparation was started by oligo(dT) priming,
868 with primers already containing the Illumina-compatible linker sequence for Read 2. After first-

869 strand synthesis, the RNA was removed before random primers that contained the corresponding
870 Illumina-compatible linker sequence for Read 1 initiated the second-strand synthesis. Second
871 strand synthesis was followed by a magnetic bead-based purification step. The libraries were
872 PCR amplified introducing sequences required for cluster generation and i7 and i5 dual indices
873 (Lexogen i7 6 nt Index Set and Lexogen i5 6 nt Unique Dual Indexing Add-on Kit) for 16-20
874 PCR cycles with the optimal number predetermined by qPCR with the PCR Add-on Kit for
875 Illumina (Lexogen GmbH). After a second magnetic bead-based purification, libraries were
876 quantified using the Qubit dsDNA HS Assay Kit (Thermo Fisher Scientific) and sized using an
877 Agilent High Sensitive D5000 Screen Tape (Agilent Technologies) to determine molarity. Equal
878 molar amounts of the libraries were multiplexed and then sequenced on an Illumina Hiseq3000
879 platform (Illumina, San Diego, CA, USA) at the Center for Genome Research and
880 Biocomputing, Oregon State University using single-end sequencing with 100-bp reads.
881 Approximately 6.6 million reads were obtained per liver sample.

882 **Sequence alignment and gene counts**

883 Adaptors and low quality tails were trimmed and ribosomal rRNA contaminations were removed
884 using BBDuk from the BBTools toolset (Bushnell, 2014). As recommended by the manufacturer
885 (Lexogen GmbH), a Phred score of 10 and a read length of 20 were used as the minimum cutoff
886 prior to data analysis (https://www.lexogen.com/quantseq-data-analysis/). Using a splice-aware
887 aligner STAR (Dobin *et al.*, 2013) (version 37.95), cleaned reads were then mapped against the
888 GRCm38 primary assembly of the *Mus musculus* genome (version mm10, M22 release)
889 (ftp://ftp.ebi.ac.uk/pub/databases/gencode/Gencode_mouse/release_M22/GRCm38.primary_asse
890 nbly.genome.fa.gz) with the annotation file of the same version
891 (ftp://ftp.ebi.ac.uk/pub/databases/gencode/Gencode_mouse/release_M22/gencode.vM22.annotati
892 on .gtf.gz), both from the GENCODE project (Frankish *et al.*, 2019). On average, over 81% of
893 the reads were uniquely mapped for each sample. Downstream analyses were based on uniquely
894 aligned reads.

895 To generate count matrices from bam files, the summarizeOverlaps function from the
896 GenomicAlignments package (v1.26.0) was used (Lawrence *et al.*, 2013). The location of the
897 exons for each gene was obtained from a transcript database (TxDb) using the
898 makeTxDbFromGFF function from the GenomicFeatures package (version 1.42.1), with a pre-

899 scanned GTF file used in the mapping step. Genes were then annotated with the R package Mus
900 musculus (version 1.3.1) (Team, 2016).

901 **Identification of differentially expressed genes (DEGs)**

902 R package edgeR (version 3.26.8) was used to detect differential change in gene expression
903 among mice on different diets (Robinson, McCarthy and Smyth, 2010). Genes expressed in at
904 least nine samples were retained using the filterByExpr function in edgeR. Unannotated genes,
905 pseudogenes and ribosomal RNA genes were also removed from downstream analyses. Gene
906 counts were then normalized with the default TMM (trimmed mean of M-values) method
907 (Robinson and Oshlack, 2010) provided by edgeR. To account for both biological and technical
908 variability, an overdispersed Poisson model and an Empirical Bayes method were used to
909 moderate the degree of overdispersion across transcripts. Genes with a false discovery rate
910 (FDR) threshold < 0.4 were used for heatmap and volcano plot analyses, whereas genes with an
911 FDR threshold < 0.05 were used in gene ontology and pathway enrichment analysis.

912 **Gene ontology and pathway enrichment analyses**

913 Gene ontology (GO) and KEGG pathway enrichment analysis was conducted using Enrichr
914 (http://amp.pharm.mssm.edu/Enrichr) (Chen *et al.*, 2013; Kuleshov *et al.*, 2016). Genes with an
915 FDR threshold < 0.05 were analyzed with GO biological process 2018 and KEGG 2019 Mouse
916 databases. Full tables can be found in the supplementary material (Supplement_File_A).

917 **Classification of RNA-seq data**

918 Gene selection and normalization were performed using the R package DaMiRseq 1.2.0 (Chiesa,
919 Colombo and Piacentini, 2018). To distinguish TXN-fed samples from HFD control samples, we
920 used a correlation cutoff of 0.4 for the partial least-squares feature selection (FSelect), and the
921 default correlation coefficient for the redundant feature removal (FReduct).

922 **Cell culture**

923 Murine 3T3-L1 pre-adipocytes were obtained from ATCC (Rockville, MD, USA). Prior to
924 treatments, cells were maintained in basic media, which consisted of high glucose DMEM
925 supplemented with 1% penicillin-streptomycin and 10% heat-inactivated FBS (Hyclone, Logan,
926 UT, USA). The cells were allowed to reach full confluence for 2 days. Differentiation was
927 induced by the addition of 0.5 µM IBMX (Sigma-Aldrich, St. Louis, MO, USA), 0.25 µM
928 dexamethasone (Sigma-Aldrich) and 10 µg/ml insulin (Sigma-Aldrich) plus the addition of

929 treatment compounds XN or TXN. After 48 h, media was removed and fresh DMEM was
930 replenished for continuing differentiation. To observe XN and TXN's effects on 3T3-L1
931 adipocyte differentiation, different concentrations were selected based on dose-response
932 experiments to identify the dose that maximized effectiveness while minimizing cell toxicity.

933 **MTT cell viability assay**

934 For cell viability experiments using the MTT assay, 3T3-L1 fibroblasts were seeded in 96-well
935 plates at a density of 15,000 cells per well in 200 µl of DMEM medium supplemented with 10%
936 FBS, 1% glutamine, 1 mM of sodium pyruvate, 100 units/mL penicillin, and 100 µg/mL
937 streptomycin. After incubating 48 h with various concentrations of XN or TXN at 37ºC in 5%
938 CO_2 atmosphere, the culture medium was removed and a solution of MTT [3-(4,5-
939 dimethylthiazol-2-yl)-2,5-diphenyltetrazolium bromide], 0.5 mg/mL in complete culture
940 medium, was added to each well. The cells were incubated with MTT for 3 h at 37ºC and then
941 the MTT medium was removed before adding acidified isopropanol to each well. The cells were
942 shaken for 10 min in an orbital shaker before reading the absorbance at 570 nm using a
943 Microplate Reader (SpectraMax 190, Molecular Devices, Sunnyvale, CA, USA). Cell viability of
944 compound-treated cells was calculated as percent absorbance of vehicle-treated control cells.

945 **Oil red O staining**

946 Cells were washed twice with phosphate-buffer saline (PBS) and then fixed with 10% formalin
947 for 30 min. Cells were then washed with ddH_2O followed by 60% isopropanol. A 0.4% stock
948 solution of Oil Red O (Sigma-Aldrich) in isopropanol was diluted 3:2 (Oil red O:ddH_2O) for a
949 working solution. To determine intracellular lipid accumulation, fixed cells were incubated for
950 30 – 60 min at room temperature on a rocker with the Oil red O working solution. After
951 incubation, cells were washed with ddH_2O and imaged using microscopy.

952 **Adipocyte gene expression by RT-qPCR**

953 Total RNA was isolated as described above, dissolved in RNase-free water and stored at -80 ºC.
954 For RT-PCR experiments, cells were grown in 6-well plates and treated with XN and TXN at 25
955 µM concentration and differentiation medium after confluence for 2 days. Gene expression was
956 measured from cells at 7 d post treatment. RNA (0.25 µg) was converted to cDNA using iScript
957 reverse transcriptase and random hexamer primers (Bio-Rad Laboratories), according to the
958 manufacturer's recommendations. PCRs were set up as described previously (Gombart,

959 Borregaard and Koeffler, 2005). All the threshold cycle number (CT) were normalized to Ywhaz
960 reference gene. PrimeTime® Std qPCR assays were purchased from IDT (**Table 5**). ΔCT =
961 CT(target gene) – CT(reference gene). ΔΔCT = ΔCT(treated sample) – ΔCT(untreated sample/control
962 average). Statistics were done on ΔΔCT values.

963 Table 5 Primer probe information

Gene Name	IDT Assay Name	RefSeq Number
Cd36	Mm.PT.58.12375764	NM_007643
Cidec/Fsp27	Mm.PT.58.6462335	NM_178373
Fabp4	Mm.PT.58.43866459	NM_024406
Fgf21	Mm.PT.58.29365871.g	NM_020013
Il6	Mm.PT.58.10005566	NM_031168
Lpl	Mm.PT.58.46006099	NM_008509
Mogat1	Mm.PT.58.41635461	NM_026713
Pparγ2	Mm.PT.58.31161924	NM_011146
Ppargc1α	Mm.PT.58.28716430	NR_027710
Plin4	Mm.PT.58.43717773	NM_020568
Scd1	Mm.PT.58.8351960	NM_009127
Srebf1	Mm.PT.58.8508227	NM_011480

964 **Time-resolved fluorescence resonance energy transfer (TR-FRET)**
965 To determine the binding affinity of XN and TXN to PPARγ, a Lanthascreen™ TR-FRET
966 PPARγ competitive binding assay was performed by Thermo Fisher Scientific as described (cite
967 manual). A terbium-labeled anti-GST antibody binds to a GST-PPARγ-ligand binding domain
968 fusion protein in which the LBD is occupied by a fluorescent pan- PPAR ligand (Fluormone™
969 Pan-PPAR Green). Energy transfer from the antibody to the ligand occurs and a high TR-FRET
970 ratio (emission signal at 520 nm/495 nm) is detected. When a test compound displaces the ligand
971 from PPARγ-LBD, a decrease in the FRET signal occurs and a lower TR-FRET ratio is detected
972 (Invitrogen Corporation, 2008). For each compound (XN, TXN or oleic acid) a 10-point serial
973 dilution (250,000 to 12.5 nM) was tested. Binding curves were generated by plotting percent
974 displacement versus log concentration (nM), and IC_{50} values were determined using a sigmoidal
975 dose response (variable slope).

976 **Molecular docking simulations for XN and TXN into the PPARγ ligand-binding domain**
977 To estimate the binding mode of XN and TXN to PPARγ, molecular docking simulations were
978 performed using AutoDock Vina (Trott and Olson, 2010). Structural models of XN and TXN

979 were built using OpenBabel to convert the isometric SMILES descriptor for XN to a PDB
980 formatted file, which was subsequently modified using PyMOL (The PyMOL Molecular
981 Graphics System, Version 1.7.4.5, Schrödinger, LLC) to obtain a PDB file for TXN. The solved
982 structure of PPARγ bound to the antagonist resveratrol (PDB ID: 4JAZ) was used as the receptor
983 model. The PDBQT files for the receptor and the resveratrol, XN, TXN, and oleic acid ligands
984 were generated using MGLTools-1.5.7rc1 (Morris *et al.*, 2009). The PPARγ receptor was kept
985 rigid during all docking experiments, and the center and size (20 x 20 x 20 $Å^3$) of the docking
986 box was positioned to cover the entire ligand-binding site of PPARγ. All rotatable torsion angles
987 in the ligand models were allowed to be active during the docking simulations. Twenty docking
988 poses were generated for each simulation, and the conformation with the lowest docking energy
989 was chosen as being representative.

990 **Statistical analysis**

991 Analysis of variance procedures for continuous data and Fisher's exact test for binary data were
992 used for statistical comparisons. P-values of orthogonal *a priori* comparisons of the HFD control
993 group versus each of the supplement groups are shown in the corresponding tables and figures.
994 Additional details of statistical analyses are described in the corresponding figure legends.

995 Acknowledgements

996 We thank Jamie Pennington, Scott Leonard and Dr. Wenbin Wu for their assistance, Dr. Edward
997 Davis for bioinformatics support and Anne-Marie Girard-Pohjanpelto, Mark Dasenko, Dr. Brent
998 Kronmiller and Matthew Peterson at the Center of Genome Research and Bioinformatics at
999 Oregon State University (OSU) for their assistance with RNA-sequencing. We thank Drs. Russ
1000 Turner and Urszula Iwaniec at the School of Biological and Population Health Sciences at OSU
1001 for use of the Lunar PIXImus 2 Dual Energy X-ray Absorptiometer (DXA) instrument. The
1002 National Institutes of Health (NIH grants 5R01AT009168 to A.F.G., C.S.M., and J.F.S. and
1003 1S10RR027878 to J.F.S.), the Linus Pauling Institute (LPI), the OSU College of Pharmacy,
1004 Hopsteiner, Inc., New York, and the OSU Foundation Buhler-Wang Research Fund supported
1005 this research. The Marion T. Tsefalas Graduate Fellowship from the LPI, the ZRT Laboratory
1006 Fund for the LPI, and the Charley Helen, Nutrition Science and Margy J. Woodburn Fellowships
1007 from the School of Biological and Population Health Sciences at OSU supported Y.Z.

1008 **References**

1009 Almeda-Valdés, P., Cuevas-Ramos, D. and Aguilar-Salinas, C. A. (2009) "Metabolic syndrome
1010 and non-alcoholic fatty liver disease," *Annals of hepatology*, 8 Suppl 1, pp. S18-24.

1011 Ammazzalorso, A. and Amoroso, R. (2019) "Inhibition of PPARγ by Natural Compounds as a
1012 Promising Strategy in Obesity and Diabetes," *The open medicinal chemistry journal*, 13(1). doi:
1013 10.2174/1874104501913010007.

1014 Bechmann, L. P. *et al.* (2012) "The interaction of hepatic lipid and glucose metabolism in liver
1015 diseases," *Journal of hepatology*, 56(4), pp. 952–964.

1016 van Beek, L. *et al.* (2015) "The limited storage capacity of gonadal adipose tissue directs the
1017 development of metabolic disorders in male C57Bl/6J mice," *Diabetologia*, 58(7), pp. 1601–
1018 1609.

1019 Bełtowski, J., Rachańczyk, J. and Włodarczyk, M. (2013) "Thiazolidinedione-induced fluid
1020 retention: recent insights into the molecular mechanisms," *PPAR research*, 2013, p. 628628.

1021 Bogue, M. A. *et al.* (2020) "Mouse Phenome Database: a data repository and analysis suite for
1022 curated primary mouse phenotype data," *Nucleic acids research*, 48(D1), pp. D716–D723.

1023 Brunt, E. M. and Tiniakos, D. G. (2010) "Histopathology of nonalcoholic fatty liver disease,"
1024 *World journal of gastroenterology: WJG*, 16(42), pp. 5286–5296.

1025 Brusotti, G. *et al.* (2017) "Betulinic acid is a PPARγ antagonist that improves glucose uptake,
1026 promotes osteogenesis and inhibits adipogenesis," *Scientific reports*, 7(1), p. 5777.

1027 Bugge, A. *et al.* (2010) "A novel intronic peroxisome proliferator-activated receptor gamma
1028 enhancer in the uncoupling protein (UCP) 3 gene as a regulator of both UCP2 and -3 expression
1029 in adipocytes," *The Journal of biological chemistry*, 285(23), pp. 17310–17317.

1030 Bushnell, B. (2014) *BBMap: a fast, accurate, splice-aware aligner*. Lawrence Berkeley National
1031 Lab.(LBNL), Berkeley, CA (United States). Available at:
1032 https://www.osti.gov/servlets/purl/1241166.

1033 Calleri, E. *et al.* (2014) "Resveratrol and its metabolites bind to PPARs," *Chembiochem: a*
1034 *European journal of chemical biology*, 15(8), pp. 1154–1160.

1035 Chao, L. *et al.* (2000) "Adipose tissue is required for the antidiabetic, but not for the
1036 hypolipidemic, effect of thiazolidinediones," *The Journal of clinical investigation*, 106(10), pp.
1037 1221–1228.

1038 Chen, E. Y. *et al.* (2013) "Enrichr: interactive and collaborative HTML5 gene list enrichment
1039 analysis tool," *BMC bioinformatics*, 14, p. 128.

1040 Chen, Z. *et al.* (2012) "Insulin resistance and metabolic derangements in obese mice are
1041 ameliorated by a novel peroxisome proliferator-activated receptor γ-sparing thiazolidinedione,"
1042 *The Journal of biological chemistry*. ASBMB, 287(28), pp. 23537–23548.

1043 Chiesa, M., Colombo, G. I. and Piacentini, L. (2018) "DaMiRseq-an R/Bioconductor package for
1044 data mining of RNA-Seq data: normalization, feature selection and classification,"
1045 *Bioinformatics* , 34(8), pp. 1416–1418.

1046 Choi, S.-S. *et al.* (2016) "PPARγ Antagonist Gleevec Improves Insulin Sensitivity and Promotes
1047 the Browning of White Adipose Tissue," *Diabetes*, 65(4), pp. 829–839.

1048 Costa, R. *et al.* (2017) "Xanthohumol and 8-prenylnaringenin ameliorate diabetic-related
1049 metabolic dysfunctions in mice," *The Journal of nutritional biochemistry*, 45, pp. 39–47.

1050 Dobin, A. *et al.* (2013) "STAR: ultrafast universal RNA-seq aligner," *Bioinformatics* , 29(1), pp.
1051 15–21.

1052 Dorn, C. *et al.* (2010) "Xanthohumol, a chalcon derived from hops, inhibits hepatic inflammation
1053 and fibrosis," *Molecular nutrition & food research*, 54 Suppl 2, pp. S205-13.

1054 Estes, C. *et al.* (2018) "Modeling the epidemic of nonalcoholic fatty liver disease demonstrates
1055 an exponential increase in burden of disease," *Hepatology* , 67(1), pp. 123–133.

1056 Fang, L. *et al.* (2016) "PPARgene: A Database of Experimentally Verified and Computationally
1057 Predicted PPAR Target Genes," *PPAR research*, 2016, p. 6042162.

1058 Fonseca, V. (2003) "Effect of thiazolidinediones on body weight in patients with diabetes
1059 mellitus," *The American journal of medicine*, 115 Suppl 8A, pp. 42S-48S.

1060 Frankish, A. *et al.* (2019) "GENCODE reference annotation for the human and mouse genomes,"
1061 *Nucleic acids research*, 47(D1), pp. D766–D773.

1062 Garcia-Jaramillo, M. *et al.* (2019) "Lipidomic and transcriptomic analysis of western diet-
1063 induced nonalcoholic steatohepatitis (NASH) in female Ldlr -/- mice," *PloS one*, 14(4), p.
1064 e0214387.

1065 Goldberg, I. J. and Ginsberg, H. N. (2006) "Ins and outs modulating hepatic triglyceride and
1066 development of nonalcoholic fatty liver disease," *Gastroenterology*, 130(4), pp. 1343–1346.

1067 Gombart, A. F., Borregaard, N. and Koeffler, H. P. (2005) "Human cathelicidin antimicrobial
1068 peptide (CAMP) gene is a direct target of the vitamin D receptor and is strongly up-regulated in
1069 myeloid cells by 1, 25-dihydroxyvitamin D3," *The FASEB journal*. FASEB, 19(9), pp. 1067–
1070 1077.

1071 Gong, Z. *et al.* (2009) "The role of tanshinone IIA in the treatment of obesity through
1072 peroxisome proliferator-activated receptor gamma antagonism," *Endocrinology*, 150(1), pp.
1073 104–113.

1074 Goto, T. *et al.* (2013) "Natural compounds regulate energy metabolism by the modulating the
1075 activity of lipid-sensing nuclear receptors," *Molecular nutrition & food research*. Wiley Online
1076 Library, 57(1), pp. 20–33.

1077 Griffin, J. D. *et al.* (2017) "Role of Hepatic PLIN2 and PLIN4 in The Development of Western
1078 Type Diet Induced Hepatosteatosis," *The FASEB Journal*. John Wiley & Sons, Ltd, 31(S1), pp.
1079 458.3-458.3.

1080 Hashimoto, E., Taniai, M. and Tokushige, K. (2013) "Characteristics and diagnosis of
1081 NAFLD/NASH," *Journal of gastroenterology and hepatology*, 28 Suppl 4, pp. 64–70.

1082 Henney, J. E. (2000) "Withdrawal of Troglitazone and Cisapride," *JAMA: the journal of the*
1083 *American Medical Association*. American Medical Association, 283(17), pp. 2228–2228.

1084 Invitrogen Corporation (2008) *LanthaScreen™ TR-FRET PPARg Assay Manual*. Carlsbad, CA,
1085 USA. Available at:
1086 https://www.thermofisher.com/order/catalog/product/PV4894?us&en#/PV4894?us&en.

1087 Ipsen, D. H., Lykkesfeldt, J. and Tveden-Nyborg, P. (2018) "Molecular mechanisms of hepatic
1088 lipid accumulation in non-alcoholic fatty liver disease," *Cellular and molecular life sciences:*
1089 *CMLS*, 75(18), pp. 3313–3327.

1090 Jia, Y. *et al.* (2012) "The natural carotenoid astaxanthin, a PPAR-α agonist and PPAR-γ
1091 antagonist, reduces hepatic lipid accumulation by rewiring the transcriptome in lipid-loaded
1092 hepatocytes," *Molecular nutrition & food research*, 56(6), pp. 878–888.

1093 Karbowska, J. and Kochan, Z. (2012) "Intermittent fasting up-regulates Fsp27/Cidec gene
1094 expression in white adipose tissue," *Nutrition* , 28(3), pp. 294–299.

1095 Kim, S.-J., Nian, C. and McIntosh, C. H. S. (2011) "Adipocyte expression of the glucose-
1096 dependent insulinotropic polypeptide receptor involves gene regulation by PPARγ and histone
1097 acetylation," *Journal of lipid research*, 52(4), pp. 759–770.

1098 Kim, Y.-J. *et al.* (2008) "Transcriptional activation of Cidec by PPARgamma2 in adipocyte,"
1099 *Biochemical and biophysical research communications*, 377(1), pp. 297–302.

1100 Kirkwood, J. S. *et al.* (2013) "A metabolomics-driven elucidation of the anti-obesity mechanisms
1101 of xanthohumol," *The Journal of biological chemistry*, 288(26), pp. 19000–19013.

1102 Kuleshov, M. V. *et al.* (2016) "Enrichr: a comprehensive gene set enrichment analysis web
1103 server 2016 update," *Nucleic acids research*, 44(W1), pp. W90-7.

1104 Kwak, H. J. *et al.* (2016) "Suppression of Adipocyte Differentiation by Foenumoside B from
1105 Lysimachia foenum-graecum Is Mediated by PPARγ Antagonism," *PloS one*, 11(5), p.
1106 e0155432.

1107 Lawrence, M. *et al.* (2013) "Software for computing and annotating genomic ranges," *PLoS*
1108 *computational biology*, 9(8), p. e1003118.

1109 Lee, J.-E. and Ge, K. (2014) "Transcriptional and epigenetic regulation of PPARγ expression
1110 during adipogenesis," *Cell & bioscience*, 4, p. 29.

1111 Lee, Y. J. *et al.* (2012) "Nuclear receptor PPARγ-regulated monoacylglycerol O-acyltransferase
1112 1 (MGAT1) expression is responsible for the lipid accumulation in diet-induced hepatic
1113 steatosis," *Proceedings of the National Academy of Sciences of the United States of America*,
1114 109(34), pp. 13656–13661.

1115 Lefterova, M. I. *et al.* (2014) "PPARγ and the global map of adipogenesis and beyond," *Trends*
1116 *in endocrinology and metabolism: TEM*, 25(6), pp. 293–302.

1117 Legette, L. *et al.* (2014) "Human pharmacokinetics of xanthohumol, an antihyperglycemic
1118 flavonoid from hops," *Molecular nutrition & food research*, 58(2), pp. 248–255.

1119 Lehmann, J. M. *et al.* (1995) "An Antidiabetic Thiazolidinedione Is a High Affinity Ligand for
1120 Peroxisome Proliferator-activated Receptor γ (PPARγ)," *The Journal of biological chemistry*,
1121 270(22), pp. 12953–12956.

1122 Li, Y.-T. *et al.* (2009) "7-Chloroarctinone-b as a new selective PPARgamma antagonist potently
1123 blocks adipocyte differentiation," *Acta pharmacologica Sinica*, 30(9), pp. 1351–1358.

1124 Lighton, J. R. B. and Halsey, L. G. (2011) "Flow-through respirometry applied to chamber
1125 systems: pros and cons, hints and tips," *Comparative biochemistry and physiology. Part A,*
1126 *Molecular & integrative physiology*, 158(3), pp. 265–275.

1127 Lytle, K. A., Wong, C. P. and Jump, D. B. (2017) "Docosahexaenoic acid blocks progression of
1128 western diet-induced nonalcoholic steatohepatitis in obese Ldlr-/- mice," *PloS one*, 12(4), p.
1129 e0173376.

1130 Mahli, A. *et al.* (2019) "Therapeutic Application of Micellar Solubilized Xanthohumol in a
1131 Western-Type Diet-Induced Mouse Model of Obesity, Diabetes and Non-Alcoholic Fatty Liver
1132 Disease," *Cells* , 8(4). doi: 10.3390/cells8040359.

1133 Matsusue, K. *et al.* (2003) "Liver-specific disruption of PPARgamma in leptin-deficient mice
1134 improves fatty liver but aggravates diabetic phenotypes," *The Journal of clinical investigation*,
1135 111(5), pp. 737–747.

1136 Matsusue, K. *et al.* (2008) "Hepatic steatosis in leptin-deficient mice is promoted by the
1137 PPARgamma target gene Fsp27," *Cell metabolism*, 7(4), pp. 302–311.

1138 Medvedev, A. V. *et al.* (2001) "Transcriptional regulation of the mouse uncoupling protein-2
1139 gene. Double E-box motif is required for peroxisome proliferator-activated receptor-gamma-
1140 dependent activation," *The Journal of biological chemistry*, 276(14), pp. 10817–10823.

1141 Miranda, C. L. *et al.* (2016) "Xanthohumol improves dysfunctional glucose and lipid metabolism
1142 in diet-induced obese C57BL/6J mice," *Archives of biochemistry and biophysics*, 599, pp. 22–30.

1143 Miranda, C. L. *et al.* (2018) "Non-estrogenic Xanthohumol Derivatives Mitigate Insulin
1144 Resistance and Cognitive Impairment in High-Fat Diet-induced Obese Mice," *Scientific reports*,
1145 8(1), p. 613.

1146 Miyata, S. *et al.* (2015) "Xanthohumol Improves Diet-induced Obesity and Fatty Liver by
1147 Suppressing Sterol Regulatory Element-binding Protein (SREBP) Activation," *The Journal of*
1148 *biological chemistry*, 290(33), pp. 20565–20579.

1149 Morris, G. M. *et al.* (2009) "AutoDock4 and AutoDockTools4: Automated docking with
1150 selective receptor flexibility," *Journal of computational chemistry*, 30(16), pp. 2785–2791.

1151 Nesto, R. W. *et al.* (2004) "Thiazolidinedione use, fluid retention, and congestive heart failure: a
1152 consensus statement from the American Heart Association and American Diabetes Association,"
1153 *Diabetes care*, 27(1), pp. 256–263.

1154 Park, S. Y. *et al.* (2008) "Cilostazol increases 3T3-L1 preadipocyte differentiation with improved
1155 glucose uptake associated with activation of peroxisome proliferator-activated receptor-γ
1156 transcription," *Atherosclerosis*, 201(2), pp. 258–265.

1157 Promrat, K. *et al.* (2004) "A pilot study of pioglitazone treatment for nonalcoholic
1158 steatohepatitis," *Hepatology* , 39(1), pp. 188–196.

1159 Ratziu, V. *et al.* (2008) "Rosiglitazone for nonalcoholic steatohepatitis: one-year results of the
1160 randomized placebo-controlled Fatty Liver Improvement with Rosiglitazone Therapy (FLIRT)
1161 Trial," *Gastroenterology*, 135(1), pp. 100–110.

1162 Ratziu, V. *et al.* (2010) "Long-term efficacy of rosiglitazone in nonalcoholic steatohepatitis:
1163 results of the fatty liver improvement by rosiglitazone therapy (FLIRT 2) extension trial,"
1164 *Hepatology* , 51(2), pp. 445–453.

1165 Rayalam, S. *et al.* (2009) "Anti-obesity effects of xanthohumol plus guggulsterone in 3T3-L1
1166 adipocytes," *Journal of medicinal food*, 12(4), pp. 846–853.

1167 Robinson, M. D., McCarthy, D. J. and Smyth, G. K. (2010) "edgeR: a Bioconductor package for
1168 differential expression analysis of digital gene expression data," *Bioinformatics* , 26(1), pp. 139–
1169 140.

1170 Robinson, M. D. and Oshlack, A. (2010) "A scaling normalization method for differential
1171 expression analysis of RNA-seq data," *Genome biology*, 11(3), p. R25.

1172 Rosen, E. D. and Spiegelman, B. M. (2006) "Adipocytes as regulators of energy balance and
1173 glucose homeostasis," *Nature*, 444(7121), pp. 847–853.

1174 Samuels, J. S., Shashidharamurthy, R. and Rayalam, S. (2018) "Novel anti-obesity effects of
1175 beer hops compound xanthohumol: role of AMPK signaling pathway," *Nutrition & metabolism*,
1176 15, p. 42.

1177 Sankella, S., Garg, A. and Agarwal, A. K. (2016) "Characterization of the Mouse and Human
1178 Monoacylglycerol O-Acyltransferase 1 (Mogat1) Promoter in Human Kidney Proximal Tubule
1179 and Rat Liver Cells," *PloS one*, 11(9), p. e0162504.

1180 Sanyal, A. J. *et al.* (2010) "Pioglitazone, vitamin E, or placebo for nonalcoholic steatohepatitis,"
1181 *The New England journal of medicine*, 362(18), pp. 1675–1685.

1182 Schwartz, A. V. (2008) "TZDs and Bone: A Review of the Recent Clinical Evidence," *PPAR*
1183 *research*, 2008, p. 297893.

1184 Schwartz, A. V. and Sellmeyer, D. E. (2007) "Thiazolidinediones: new evidence of bone loss,"
1185 *The Journal of clinical endocrinology and metabolism*, pp. 1232–1234.

1186 Sharma, A. M. and Staels, B. (2007) "Review: Peroxisome proliferator-activated receptor
1187 gamma and adipose tissue--understanding obesity-related changes in regulation of lipid and
1188 glucose metabolism," *The Journal of clinical endocrinology and metabolism*, 92(2), pp. 386–
1189 395.

1190 Soccio, R. E., Chen, E. R. and Lazar, M. A. (2014) "Thiazolidinediones and the promise of
1191 insulin sensitization in type 2 diabetes," *Cell metabolism*, 20(4), pp. 573–591.

1192 Speakman, J. R. (2013) "Measuring energy metabolism in the mouse - theoretical, practical, and
1193 analytical considerations," *Frontiers in physiology*, 4, p. 34.

1194 Stefan, N., Häring, H.-U. and Cusi, K. (2019) "Non-alcoholic fatty liver disease: causes,
1195 diagnosis, cardiometabolic consequences, and treatment strategies," *The lancet. Diabetes &*
1196 *endocrinology*, 7(4), pp. 313–324.

1197 Strathmann, J. and Gerhauser, C. (2012) "Anti-proliferative and Apoptosis-Inducing Properties
1198 of Xanthohumol, a Prenylated Chalcone from Hops (Humulus lupulus L.)," in Diederich, M. and
1199 Noworyta, K. (eds.) *Natural compounds as inducers of cell death: volume 1*. Dordrecht: Springer
1200 Netherlands, pp. 69–93.

1201 Takahashi, K. and Osada, K. (2017) "Effect of Dietary Purified Xanthohumol from Hop
1202 (Humulus lupulus L.) Pomace on Adipose Tissue Mass, Fasting Blood Glucose Level, and Lipid
1203 Metabolism in KK-Ay Mice," *Journal of oleo science*, 66(5), pp. 531–541.

1204 Tamori, Y. *et al.* (2002) "Role of peroxisome proliferator-activated receptor-gamma in
1205 maintenance of the characteristics of mature 3T3-L1 adipocytes," *Diabetes*, 51(7), pp. 2045–
1206 2055.

1207 Team, B. C. (2016) "Mus. musculus: Annotation package for the Mus. musculus object," *R*
1208 *package version*, 1(1).

1209 Trott, O. and Olson, A. J. (2010) "AutoDock Vina: improving the speed and accuracy of docking
1210 with a new scoring function, efficient optimization, and multithreading," *Journal of*
1211 *computational chemistry*, 31(2), pp. 455–461.

1212 Tschöp, M. H. *et al.* (2011) "A guide to analysis of mouse energy metabolism," *Nature methods*,
1213 9(1), pp. 57–63.

1214 Wahlström, A. *et al.* (2016) "Intestinal Crosstalk between Bile Acids and Microbiota and Its
1215 Impact on Host Metabolism," *Cell metabolism*, 24(1), pp. 41–50.

1216 Weir, J. B. D. E. B. (1949) "New methods for calculating metabolic rate with special reference to
1217 protein metabolism," *The Journal of physiology*, 109(1–2), pp. 1–9.

1218 Wolf Greenstein, A. *et al.* (2017) "Hepatocyte-specific, PPARγ-regulated mechanisms to
1219 promote steatosis in adult mice," *The Journal of endocrinology*, 232(1), pp. 107–121.

1220 Yang, J.-Y. *et al.* (2007) "Effect of xanthohumol and isoxanthohumol on 3T3-L1 cell apoptosis
1221 and adipogenesis," *Apoptosis: an international journal on programmed cell death*, 12(11), pp.
1222 1953–1963.

1223 Yang, T. and Soodvilai, S. (2008) "Renal and vascular mechanisms of thiazolidinedione-induced
1224 fluid retention," *PPAR research*, 2008, p. 943614.

1225 Younossi, Z. M. *et al.* (2016) "Global epidemiology of nonalcoholic fatty liver disease-Meta-
1226 analytic assessment of prevalence, incidence, and outcomes," *Hepatology* , 64(1), pp. 73–84.

1227 Yui, K., Kiyofuji, A. and Osada, K. (2014) "Effects of xanthohumol-rich extract from the hop on
1228 fatty acid metabolism in rats fed a high-fat diet," *Journal of oleo science*, 63(2), pp. 159–168.

1229 Zhang, Y. *et al.* (2014) "Protopanaxatriol, a novel PPARγ antagonist from Panax ginseng,
1230 alleviates steatosis in mice," *Scientific reports*, 4, p. 7375.

1231 Zhang, Y. *et al.* (2016) "Dietary component isorhamnetin is a PPARγ antagonist and ameliorates
1232 metabolic disorders induced by diet or leptin deficiency," *Scientific reports*, 6, p. 19288.

1233 Zhang, Y. *et al.* (2020) "Improvements in Metabolic Syndrome by Xanthohumol Derivatives Are
1234 Linked to Altered Gut Microbiota and Bile Acid Metabolism," *Molecular nutrition & food*
1235 *research*, 64(1), p. e1900789.

1236 Zhu, Y. *et al.* (1993) "Cloning of a new member of the peroxisome proliferator-activated
1237 receptor gene family from mouse liver," *The Journal of biological chemistry*, 268(36), pp.
1238 26817–26820.

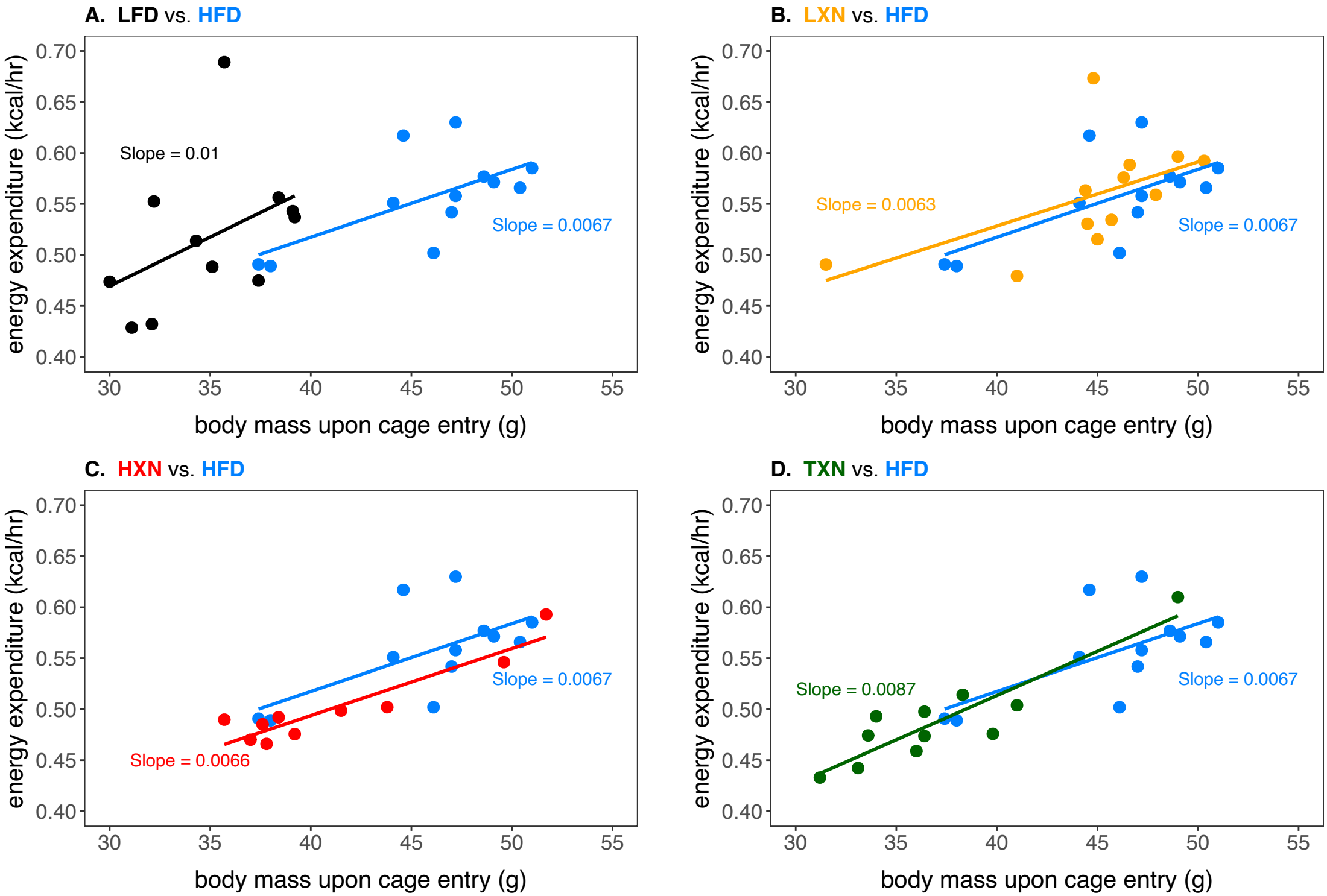
A. LFD vs. HFD
Slope = 0.01
Slope = 0.0067
B. LXN vs. HFD
Slope = 0.0063
Slope = 0.0067
C. HXN vs. HFD
Slope = 0.0067
Slope = 0.0066
D. TXN vs. HFD
Slope = 0.0087
Slope = 0.0067
energy expenditure (kcal/hr)
0.40
0.45
0.50
0.55
0.60
0.65
0.70
body mass upon cage entry (g)
30
35
40
45
50
55

Figure 3-supplement 1. Relationship of body mass and energy expenditure between (A) LFD and HFD; (B) LXN and HFD; (C) HXN and HFD; (D) TXN and HFD. Energy expenditure was measured between weeks 10 to 14. Data was analyzed using analysis of covariance (ANCOVA) of body mass upon entry into the cages and diet. No statistically significant effect from treatments was detected. HFD data are from the same group of mice and are displayed as a reference on all four panels. Source files of data used for the analysis are available in the Figure supplement 1—source data 1.

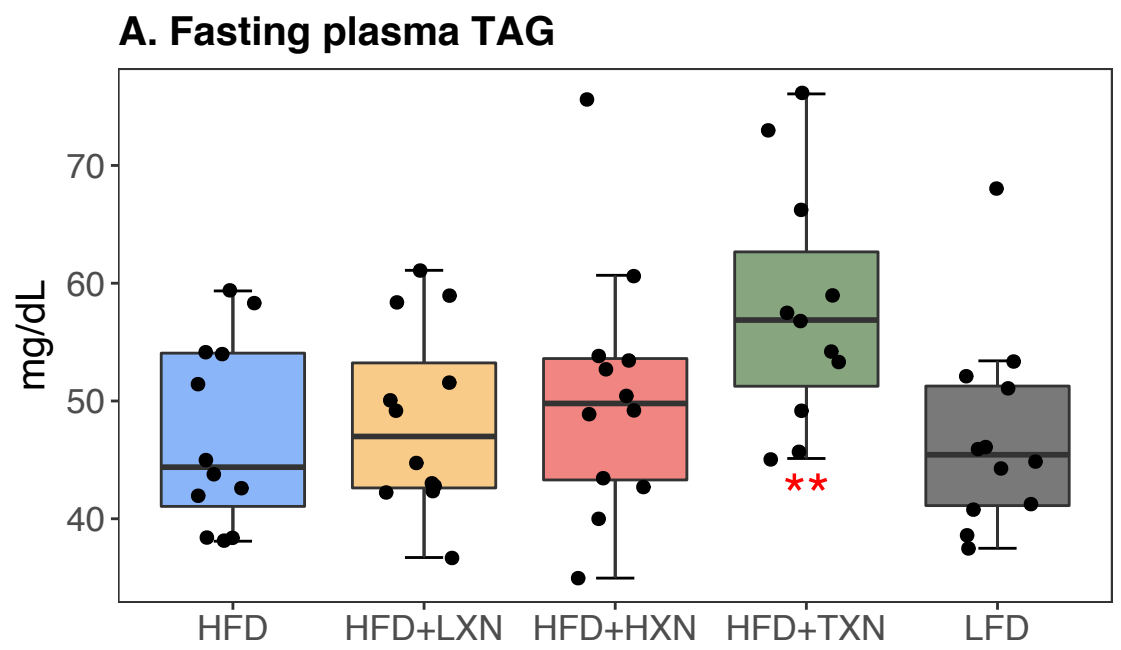
A. Fasting plasma TAG
mg/dL
70
60
50
40
**
HFD
HFD+LXN
HFD+HXN
HFD+TXN
LFD

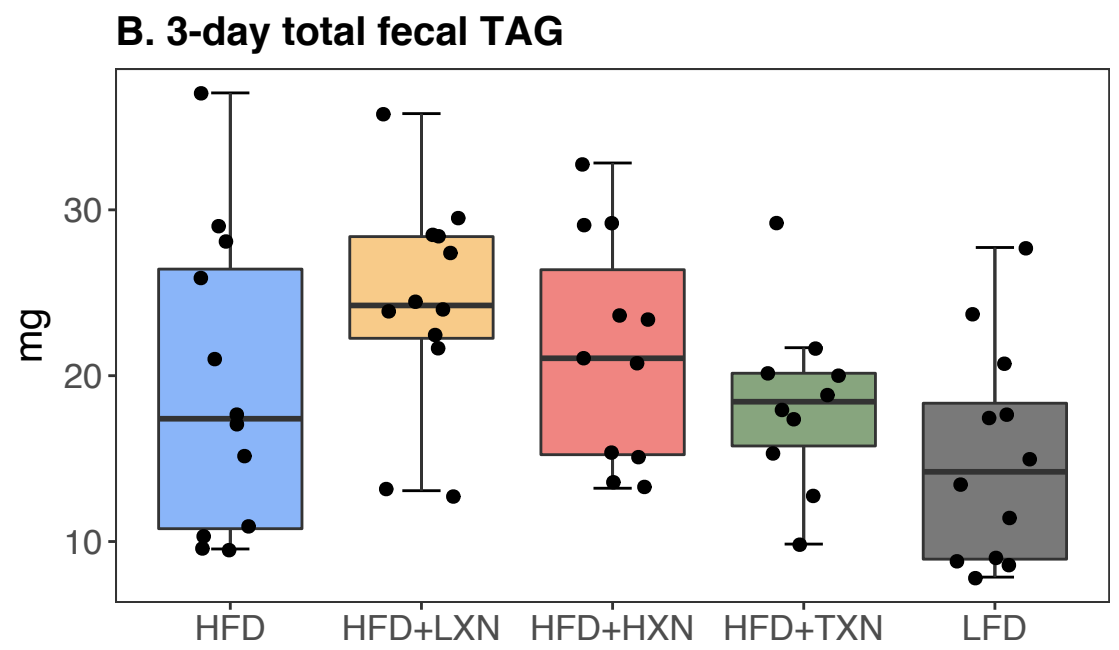
B. 3-day total fecal TAG
mg
30
20
10
HFD
HFD+LXN
HFD+HXN
HFD+TXN
LFD

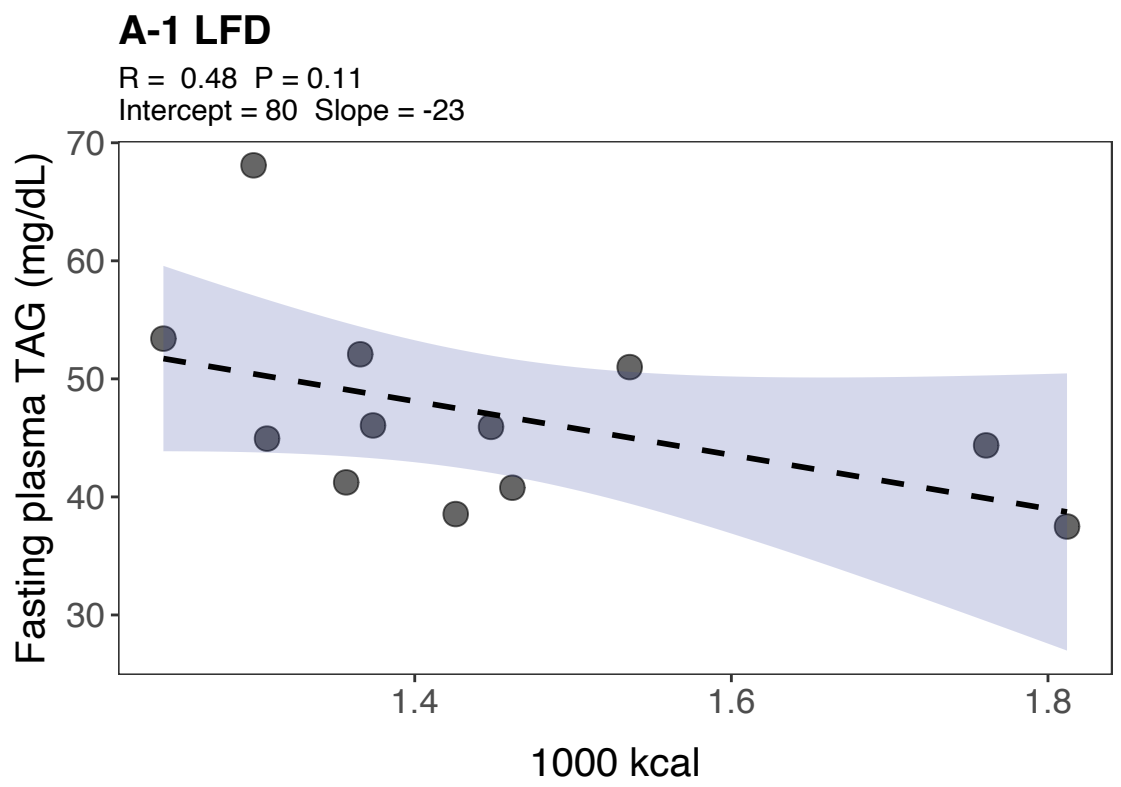
A-1 LFD
R = 0.48 P = 0.11
Intercept = 80 Slope = -23
Fasting plasma TAG (mg/dL)
70
60
50
40
30
1.4
1.6
1.8
1000 kcal

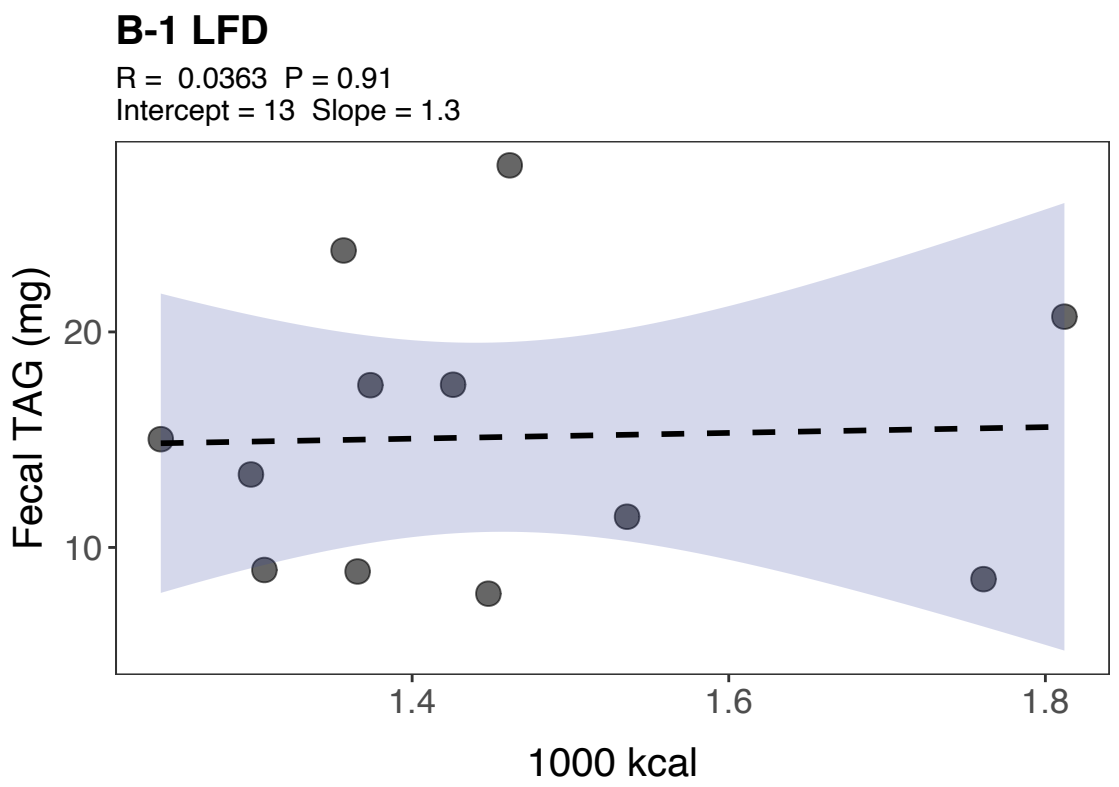
B-1 LFD
R = 0.0363 P = 0.91
Intercept = 13 Slope = 1.3
Fecal TAG (mg)
20
10
1.4
1.6
1.8
1000 kcal

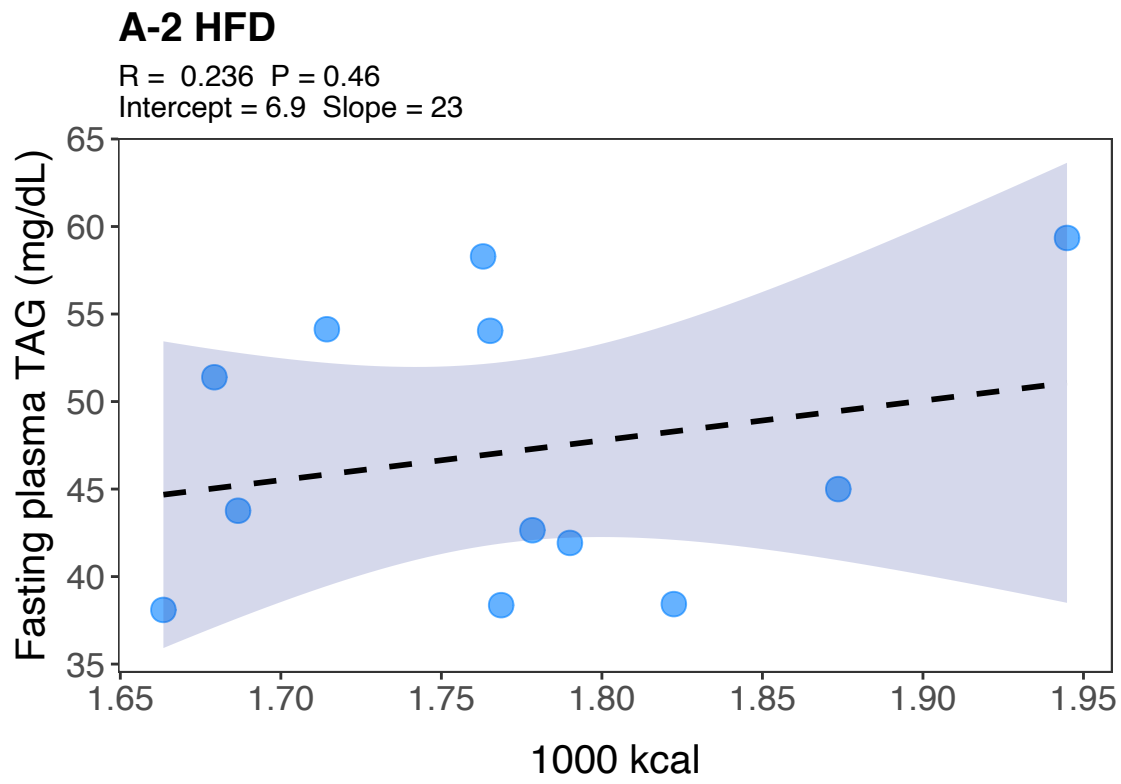
A-2 HFD
R = 0.236 P = 0.46
Intercept = 6.9 Slope = 23
Fasting plasma TAG (mg/dL)
65
60
55
50
45
40
35
1.65
1.70
1.75
1.80
1.85
1.90
1.95
1000 kcal

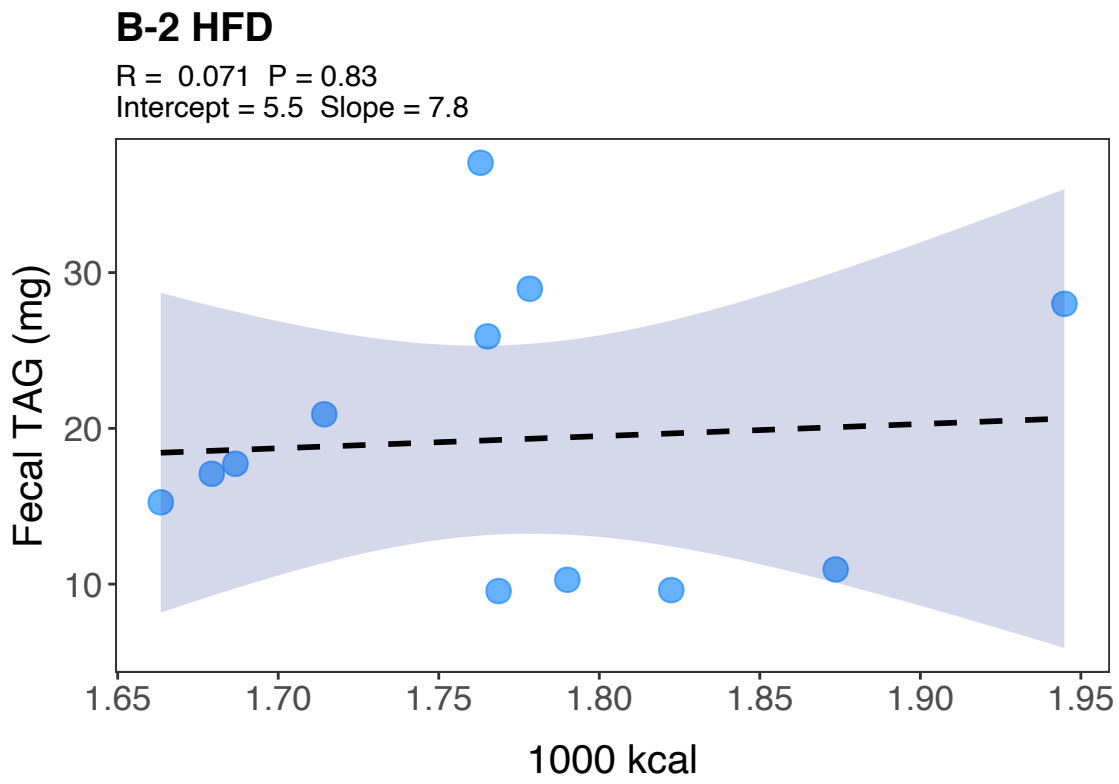
B-2 HFD
R = 0.071 P = 0.83
Intercept = 5.5 Slope = 7.8
Fecal TAG (mg)
30
20
10
1.65
1.70
1.75
1.80
1.85
1.90
1.95
1000 kcal

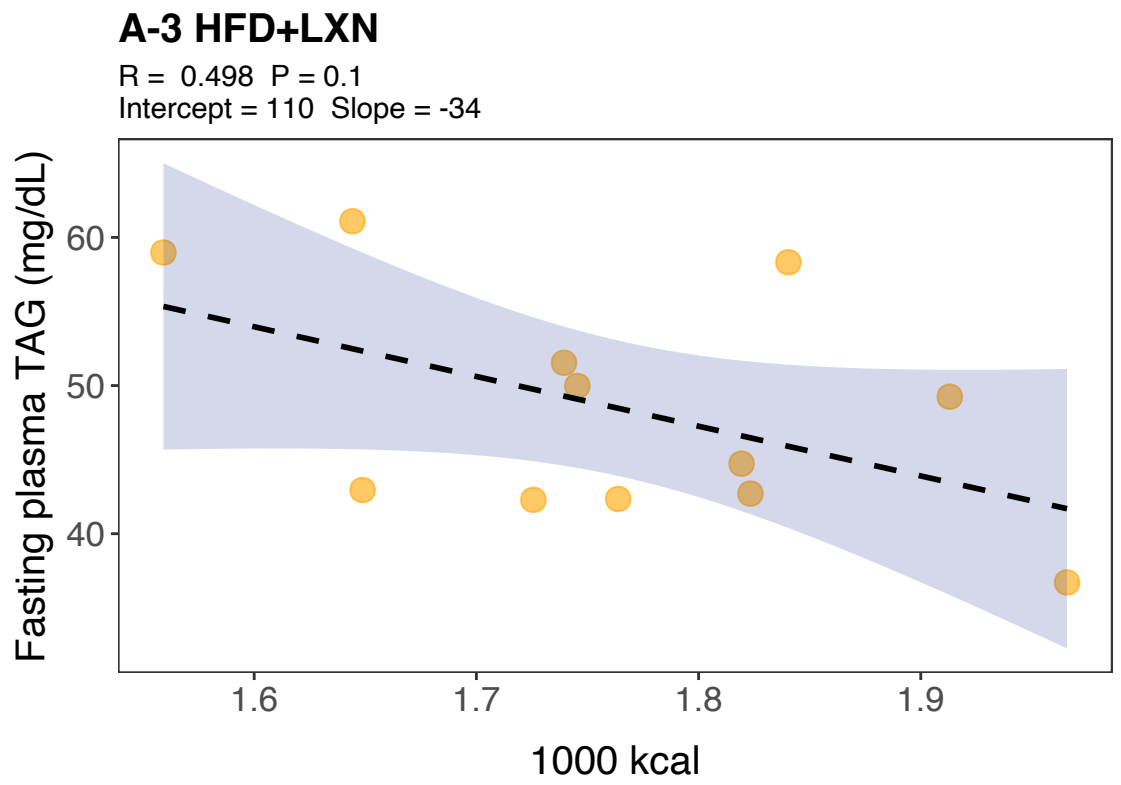
A-3 HFD+LXN
R = 0.498 P = 0.1
Intercept = 110 Slope = -34
Fasting plasma TAG (mg/dL)
60
50
40
1.6
1.7
1.8
1.9
1000 kcal

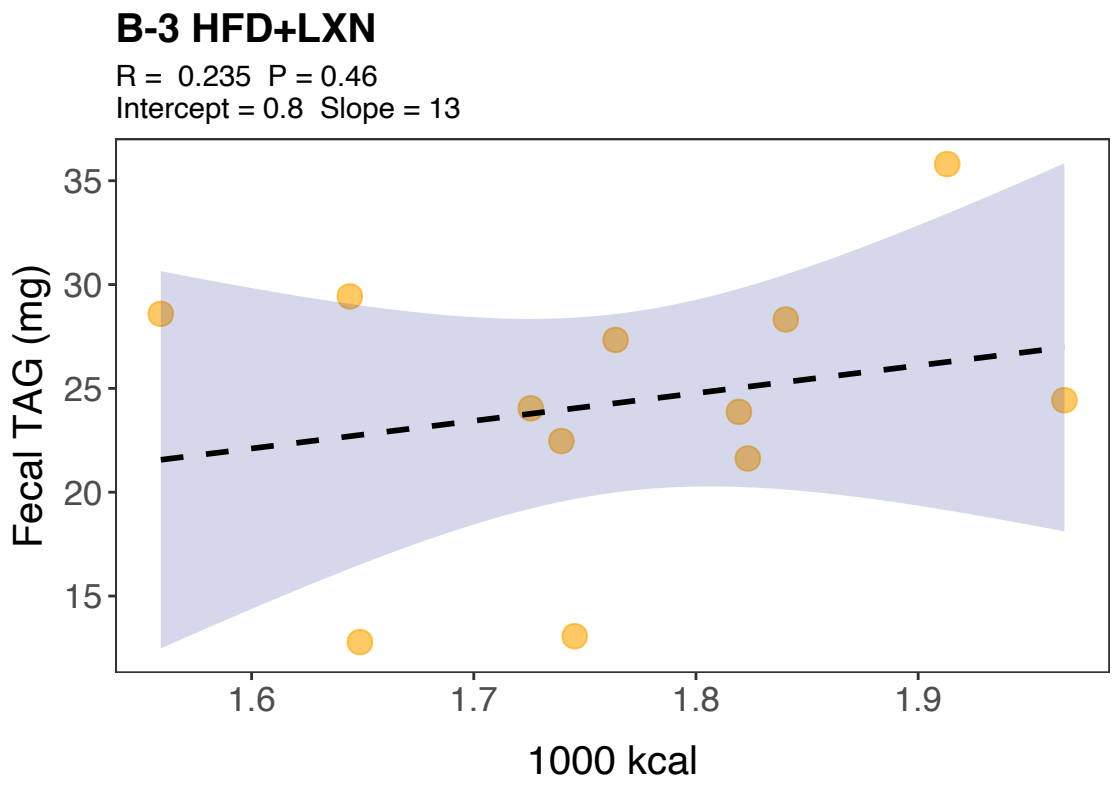
B-3 HFD+LXN
R = 0.235 P = 0.46
Intercept = 0.8 Slope = 13
Fecal TAG (mg)
35
30
25
20
15
1.6
1.7
1.8
1.9
1000 kcal

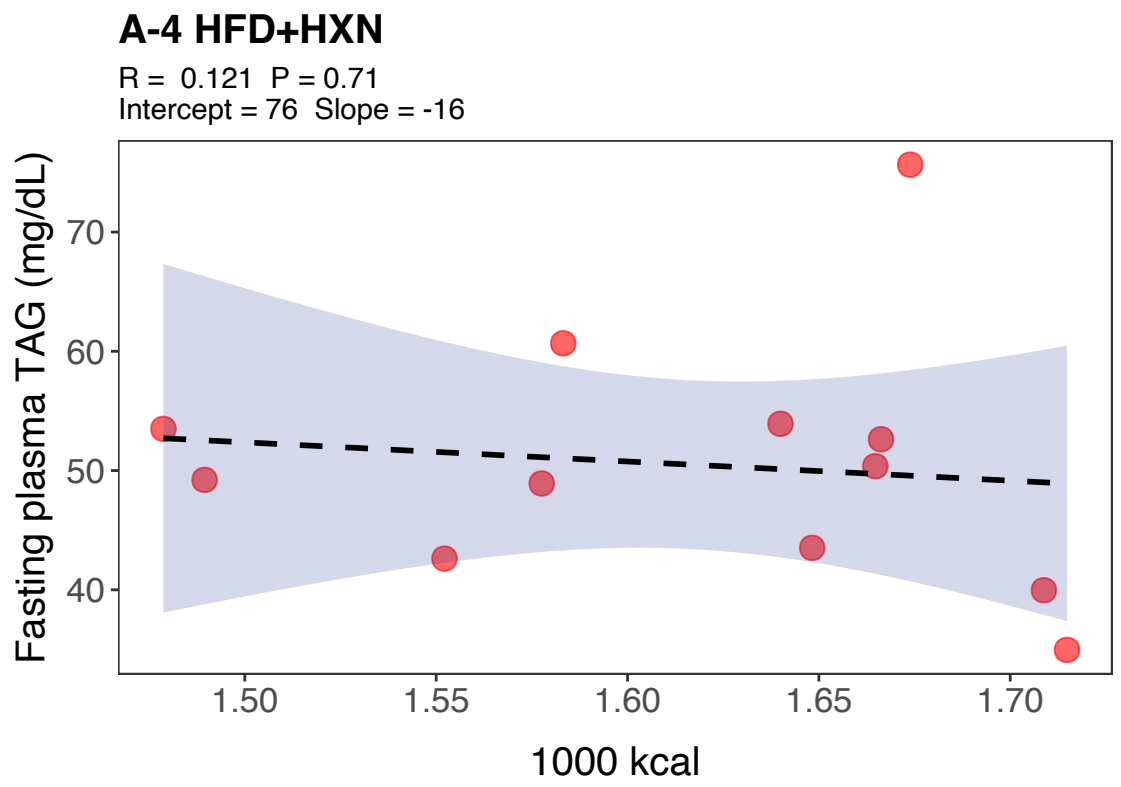
A-4 HFD+HXN
R = 0.121 P = 0.71
Intercept = 76 Slope = -16
Fasting plasma TAG (mg/dL)
70
60
50
40
1.50
1.55
1.60
1.65
1.70
1000 kcal

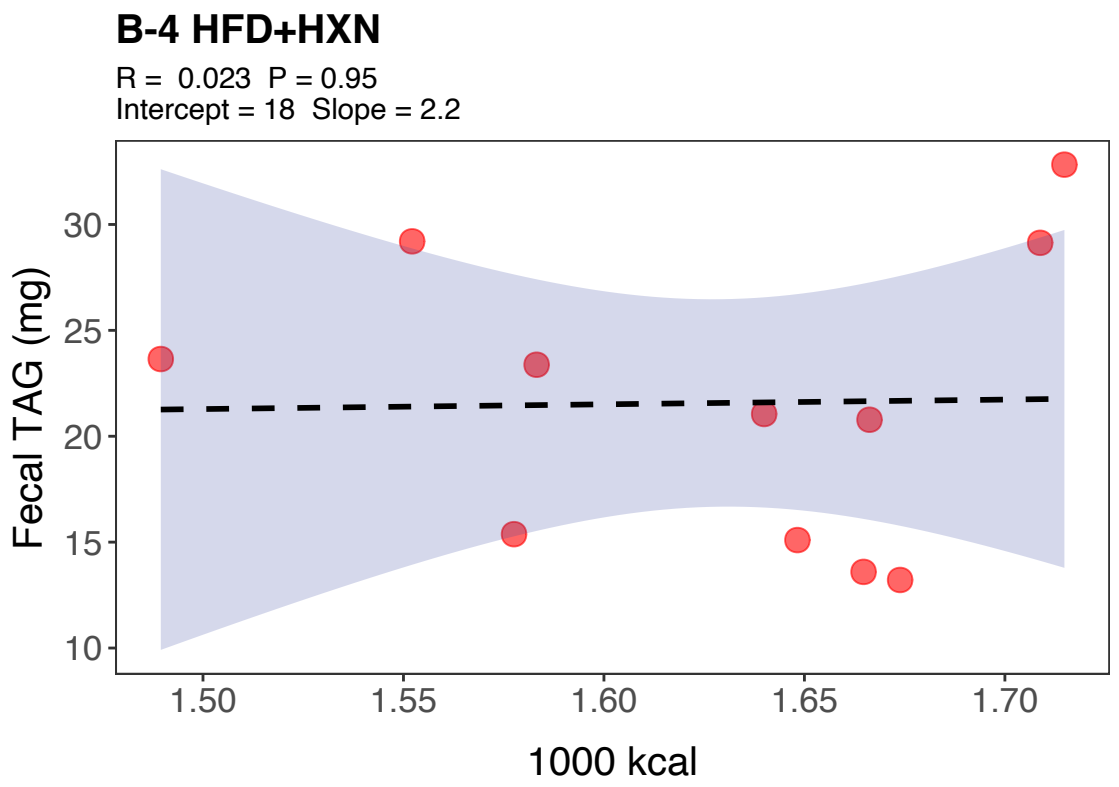
B-4 HFD+HXN
R = 0.023 P = 0.95
Intercept = 18 Slope = 2.2
Fecal TAG (mg)
30
25
20
15
10
1.50
1.55
1.60
1.65
1.70
1000 kcal

A-5 HFD+TXN
R = 0.544 P = 0.084
Intercept = 100 Slope = -24
Fasting plasma TAG (mg/dL)
70
60
50
40
1.6
1.8
2.0
1000 kcal

B-5 HFD+TXN
R = 0.525 P = 0.12
Intercept = -3.5 Slope = 13
Fecal TAG (mg)
30
25
20
15
10
1.6
1.8
2.0
1000 kcal

Figure 3-supplement 2. The effect of diet and intervention on fasting plasma and fecal TAG levels. Mice were fed either a LFD (black, n = 12), a HFD (blue, n = 12), HFD+LXN (yellow, n = 12), HFD+HXN (red, n = 12), or HFD+TXN (green, n = 11) for 16 weeks. (A) Fasting plasma TAG levels are expressed as quartiles. (A-1) Relationship between fasting plasma TAG and total caloric intake over 16 weeks of feeding for LFD group; (A-2) for HFD group; (A-3) for HFD+LXN group; (A-4) for HFD+HXN group; (A-5) for HFD+TXN group (B) 3-day total fecal triglyceride (TAG) are expressed as quartiles. (B-1) Relationship between 3-day fecal TAG and total caloric intake over 16 weeks of feeding for LFD group; (B-2) for HFD group; (B-3) for HFD+LXN group; (B-4) for HFD+HXN group; (B-5) for HFD+TXN group. Pre-planned general linear model with contrasts were used to calculate *p*-values in A, B and C. *$p < 0.05$, **$p < 0.01$, ***$p < 0.001$. Linear regression analyses of total calories versus fasting plasma TAG (A1-5) or total fecal TAG (B1-5) in mice were done using lm function of stats package version 3.6.2 in R. Blue shading represents 95% CI of the regression line. Absolute value of R, p-value, intercept, and slope for the regression are reported above each corresponding panel.